

Global adjoint tomography: first-generation model

Ebru Bozdag,¹ Daniel Peter,² Matthieu Lefebvre,³ Dimitri Komatitsch,⁴ Jeroen Tromp,^{3,5} Judith Hill,⁶ Norbert Podhorszki⁶ and David Pugmire⁶

¹Laboratory Géoazur, University of Nice Sophia Antipolis, F-06560 Valbonne, France. E-mail: bozdag@geoazur.unice.fr

²Extreme Computing Research Center, King Abdullah University of Science and Technology (KAUST), Thuwal 23955-6900, Saudi Arabia

³Department of Geosciences, Princeton University, Princeton, NJ 08544, USA

⁴LMA, CNRS UPR 7051, Aix-Marseille University, Centrale Marseille, F-13453 Marseille Cedex 13, France

⁵Program in Applied and Computational Mathematics, Princeton University, Princeton, NJ 08544, USA

⁶Oak Ridge National Laboratory, Oak Ridge, TN 37831, USA

Accepted 2016 September 21. Received 2016 September 19; in original form 2016 June 9

SUMMARY

We present the first-generation global tomographic model constructed based on adjoint tomography, an iterative full-waveform inversion technique. Synthetic seismograms were calculated using GPU-accelerated spectral-element simulations of global seismic wave propagation, accommodating effects due to 3-D anelastic crust & mantle structure, topography & bathymetry, the ocean load, ellipticity, rotation, and self-gravitation. Fréchet derivatives were calculated in 3-D anelastic models based on an adjoint-state method. The simulations were performed on the Cray XK7 named ‘Titan’, a computer with 18 688 GPU accelerators housed at Oak Ridge National Laboratory. The transversely isotropic global model is the result of 15 tomographic iterations, which systematically reduced differences between observed and simulated three-component seismograms. Our starting model combined 3-D mantle model S362ANI with 3-D crustal model Crust2.0. We simultaneously inverted for structure in the crust and mantle, thereby eliminating the need for widely used ‘crustal corrections’. We used data from 253 earthquakes in the magnitude range $5.8 \leq M_w \leq 7.0$. We started inversions by combining ~ 30 s body-wave data with ~ 60 s surface-wave data. The shortest period of the surface waves was gradually decreased, and in the last three iterations we combined ~ 17 s body waves with ~ 45 s surface waves. We started using 180 min long seismograms after the 12th iteration and assimilated minor- and major-arc body and surface waves. The 15th iteration model features enhancements of well-known slabs, an enhanced image of the Samoa/Tahiti plume, as well as various other plumes and hotspots, such as Caroline, Galapagos, Yellowstone and Erebus. Furthermore, we see clear improvements in slab resolution along the Hellenic and Japan Arcs, as well as subduction along the East of Scotia Plate, which does not exist in the starting model. Point-spread function tests demonstrate that we are approaching the resolution of continental-scale studies in some areas, for example, underneath Yellowstone. This is a consequence of our multiscale smoothing strategy in which we define our smoothing operator as a function of the approximate Hessian kernel, thereby smoothing gradients less wherever we have good ray coverage, such as underneath North America.

Key words: Body waves; Surface waves and free oscillations; Seismic anisotropy; Seismic tomography; Computational seismology; Wave propagation; Waveform inversion.

1 INTRODUCTION

Since the inception of global seismic imaging (Aki *et al.* 1977; Dziewoński *et al.* 1977; Sengupta & Toksöz 1977), many models of the mantle have been published based on various types of data, such as body-wave arrival times (e.g. Dziewoński 1984; Bijwaard & Spakman 2000; Boschi & Dziewoński 2000; Zhou *et al.* 2006), surface-wave dispersion (e.g. Trampert & Woodhouse

1995; Ekström *et al.* 1997; Shapiro & Ritzwoller 2002; Trampert & Woodhouse 2003; Ekström 2011), shear and surface waveforms (e.g. Woodhouse & Dziewoński 1984; Li & Romanowicz 1996; Lebedev & van der Hilst 2008; Schaeffer & Lebedev 2013) and the Earth’s free oscillations (e.g. He & Tromp 1996; Koelemeijer *et al.* 2016). The steady increase in the number of worldwide seismographic stations combined with improvements in data quality have substantially grown the amount of usable data for the construction

of global Earth models, and, at long wavelengths, global shear-wave-speed models are now in general agreement (e.g. Ritzwoller & Lavey 1995; Trampert & Woodhouse 2001; Becker & Boschi 2002). Several recent global studies have capitalized on this wealth of data (e.g. Ritsema *et al.* 1999; Mégnin & Romanowicz 2000; Gu *et al.* 2001; Houser *et al.* 2008; Kustowski *et al.* 2008; Ritsema *et al.* 2011; Schaeffer & Lebedev 2013; Chang *et al.* 2014), using a broad range of body-wave, surface-wave, and normal-mode observations. Ray-based (infinite-frequency) tomographic inversions have reached their theoretical limits (Wang & Dahlen 1995; Spetzler *et al.* 2001). Finite-frequency effects for surface waves were recognized much earlier (Woodhouse & Gurnis 1982; Snieder 1993) than for body waves (Marquering *et al.* 1999). Finite-frequency theory is now widely applied and has been used in global surface- (e.g. Zhou *et al.* 2006) and body-wave (e.g. Montelli *et al.* 2004) tomography. All these studies are based on tomographic methods rooted in perturbation theory of one form or another.

Current global inversions are severely limited by ‘crustal corrections’, which involve first-order corrections to accommodate the effects of Earth’s 3-D crust on seismic waves. The crust varies in thickness by an order of magnitude, from ~ 7 km below the oceans to ~ 70 km beneath the Andes and Tibet. The highly nonlinear effects of the crust on seismic wave propagation, even at long periods (Montagner & Jobert 1988), make crustal corrections questionable because they likely contaminate inferred mantle structure (e.g. Bozdağ & Trampert 2008; Lekić *et al.* 2010; Ferreira *et al.* 2010).

Despite readily available vast amounts of data, the number of measurements used in classical tomography is limited to arrivals which are easily identified and isolated in seismograms. It is common to use traveltimes of major body-wave arrivals (e.g. P , PP , S , SS , ScS , etc.), Love & Rayleigh surface-wave dispersion measurements, or very long period free oscillations. Since different parts of a seismogram are sensitive to different parts of Earth’s interior, it is also common to integrate complementary data sets. One of the major challenges in global tomography is data coverage due to the uneven distribution of earthquakes and stations. Without permanent ocean-bottom seismographic instruments, it is difficult to change this distribution. However, extracting more information from seismograms will enhance global coverage, for example, by using more exotic—but often prominent—arrivals, such as PS , SP , $PKKP$ and ScS reverberations. Ideally, complete three-component seismograms should be used in global inversions, without worrying about identifying which specific waveforms we are dealing with. Basically, any wiggle in a seismogram should make a suitable measurement, not just the ones we can readily identify with a known phase.

Recent advances in numerical methods combined with developments in high-performance computing have enabled unprecedented simulations of seismic wave propagation in realistic 3-D global Earth models (Komatitsch & Tromp 2002a,b; Capdeville *et al.* 2003; Chaljub *et al.* 2003; Chaljub & Valette 2004; Peter *et al.* 2011). In a complementary development, adjoint-state methods efficiently incorporate the full nonlinearity of 3-D wave propagation in iterative seismic inversions (Akçelik *et al.* 2002, 2003; Tromp *et al.* 2005; Fichtner *et al.* 2006a,b; Tromp *et al.* 2008; Plessix 2009; Virieux & Operto 2009; Monteiller *et al.* 2015; Komatitsch *et al.* 2016). ‘Adjoint tomography’ provides new opportunities for improving images of Earth’s interior for the following reasons: (1) the full nonlinearity of 3-D seismic wave propagation is taken into account; (2) 3-D background models are used to compute Fréchet derivatives, thereby accommodating nonlinearities due to structure; (3) data may be assimilated based on automated measurement window-selection

algorithms (Maggi *et al.* 2009; Lee & Chen 2013); (4) as a result of (1)–(3), the amount of usable data steadily increases from iteration to iteration, thus enabling the extraction of more information from seismograms, ultimately culminating in global ‘full-waveform inversion’ (FWI), that is, the use of entire three-component seismograms; and (5) the crust and mantle are inverted jointly, thereby eliminating the need for crustal corrections. The goal of this study is to harness 3-D simulations of seismic wave propagation in combination with adjoint-state methods to image the crust and mantle.

Although the basic theory of adjoint methods (Chavent 1974) for seismic inversions was introduced in the 80s (Bamberger *et al.* 1977; Lailly 1983; Tarantola 1984a,b; Gauthier *et al.* 1986; Tarantola 1988; Talagrand & Courtier 1987), their application has only recently become possible with the availability of 3-D wave propagation solvers and high-performance computing resources. Currently, there are successful applications of adjoint tomography both on regional and continental scales (Tape *et al.* 2009; Fichtner *et al.* 2009, 2013; Zhu *et al.* 2012, 2013; Zhu & Tromp 2013; Lee *et al.* 2014; Chen *et al.* 2015), however, so far it has remained a challenge in global tomography.

At the scale of the globe, the most advanced inversions to date combine 3-D spectral-element simulations of wave propagation in the mantle coupled with a normal-mode solution in a spherically symmetric core (Capdeville *et al.* 2003; Lekić & Romanowicz 2011; French *et al.* 2013; French & Romanowicz 2014). This compromise reduces the computational burden, but such coupled simulations do not accommodate Earth’s ellipticity and rotation. Additionally, meshing the Earth’s crust is avoided by replacing it with a smooth anisotropic spherical shell which mimics the behaviour of the actual crust, which is iteratively updated. Furthermore, Fréchet derivatives in the inverse problem are calculated based on the perturbation theory developed by Li & Romanowicz (1996). This hybrid approach has resulted in remarkable images of numerous mantle plumes (French & Romanowicz 2015). We note, however, that Valentine & Trampert (2016) recently reported that hybrid methods may be more error-prone than classical approximate methods. In this paper, no approximations—other than the use of a numerical method for simulating seismic wave propagation—are made in either forward or adjoint simulations and the entire globe is accommodated within a single framework, in which the crust, mantle, and core are all treated equally. A similar approach at the global scale has recently been demonstrated in a multiscale framework by Afanasiev *et al.* (2015), who performed two iterations with a smaller set of long-period data.

Success of the inversion strategy is closely tied to the choice of misfit function (e.g. Modrak & Tromp 2016). Common measures of misfit include cross-correlation traveltime measurements (e.g. Luo & Schuster 1991; Marquering *et al.* 1999; Dahlen *et al.* 2000; Zhao *et al.* 2000), multitaper phase measurements (e.g. Zhou *et al.* 2004), relative amplitude variations (e.g. Dahlen & Baig 2002; Ritsema *et al.* 2002), waveform differences (e.g. Tarantola 1984a,b, 1988; Nolet 1987), generalized seismological data functionals (GSDF) (Gee & Jordan 1992), or more recently proposed time-frequency analysis (e.g. Kristekova *et al.* 2006; Fichtner *et al.* 2008) and instantaneous phase & envelope misfits (e.g. Bozdağ *et al.* 2011; Rickers *et al.* 2012); the latter allow separation of phase and amplitude and use of long wave trains. In this study, we use frequency-dependent cross-correlation traveltimes—also called multitaper traveltime measurements—whenever we have dispersive signals, and classical cross-correlation traveltimes for non-dispersive body-wave arrivals. This facilitates an inversion for transversely isotropic lateral heterogeneity. In future studies, we will also

include cross-correlation and multitaper amplitude measurements, thereby enabling inversions that accommodate attenuation.

This paper is organized as follows. We begin by discussing the choice of the starting model, followed by a description of the data set. We then describe the inversion strategy and workflow in some detail, before discussing the first-generation global model based on adjoint tomography. We conclude by discussing our results in the broader context of the current status of global seismic tomography, and highlight a number of future research directions.

2 STARTING MODEL

It is well known that FWIs depend on the starting model. This issue has been addressed in many studies by selecting appropriate initial models and making suitable measurements to avoid getting stuck in a local minimum (e.g. Pratt & Shipp 1999; Brossier *et al.* 2009; Prieux *et al.* 2013; Yuan & Simons 2014; Yuan *et al.* 2015). Alternatively, taking advantage of broad-band seismic signals in earthquake seismology, nonlinearities may be avoided by starting with smooth models and long-period signals, and gradually increasing the frequency content in successive iterations (e.g. Nolet *et al.* 1986; Zhu *et al.* 2012; Pageot *et al.* 2013). Unfortunately, a paucity of low-frequency data makes this strategy more difficult in exploration seismology. The 1-D radial structure of the Earth is quite well known, and there is also a basic consensus on the long-wavelength shear-wave-speed structure of the mantle (e.g. Ritzwoller & Lavey 1995; Becker & Boschi 2002). Recent iterative inversions starting from radially symmetric models confirm said consensus (e.g. Lekić & Romanowicz 2011). Furthermore, reasonable global crustal models are now available, such as $2^\circ \times 2^\circ$ Crust2.0 (Basson *et al.* 2000) and its successor Crust1.0 (Laske *et al.* 2013) with $1^\circ \times 1^\circ$ resolution.

For these reasons, we decided to use a starting model that combines 3-D mantle model S362ANI (Kustowski *et al.* 2008) with 3-D crustal model Crust2.0 (Basson *et al.* 2000); we label it S362ANI+Crust2.0 in what follows.

S362ANI was constructed using surface-wave phase speeds, body-wave traveltimes, and long-period body and mantle waveforms. It has transverse isotropy in the upper mantle down to 420 km. Adding Crust2.0 (Basson *et al.* 2000) on top of mantle model S362ANI (Kustowski *et al.* 2008) poses a challenge, because S362ANI is defined in a spherical shell with bounding radii determined by the core–mantle boundary (CMB) and the PREM Moho. Thus, S362ANI needs to be stretched (underneath the oceans) and squished (underneath the continents) to ‘glue’ it onto Crust2.0 (any other global model poses a similar ‘gluing’ challenge). This procedure affects surface wave speeds, and is another motivation for jointly inverting crust and mantle structure.

We have extensive experience with this starting model, which has been used for near real-time global ShakeMovie simulations since 2010 (Tramp *et al.* 2010). There are currently more than 4700 earthquakes in the ShakeMovie database, providing 1-D (PREM) and 3-D (S362ANI+Crust2.0) synthetic seismograms for each event. This model already provides a decent fit to long-period body and surface waves ($T > 60$ s), and is a significant improvement over a 1-D model.

3 EARTHQUAKES AND SOURCE INVERSIONS

We selected waveform data for 253 earthquakes in the moment-magnitude range $5.8 \leq M_w \leq 7.0$, as shown in Fig. 1(A). The events

were chosen to provide broad geographical coverage, including shallow (depth ≤ 50 km), intermediate (50 km $>$ depth $>$ 300 km), and deep (depth ≥ 300 km) events. Because we used relatively long-period data (>17 s) and events with magnitudes less than 7, we chose a Centroid Moment-Tensor (CMT) point-source earthquake representation. We used four $M_w = 5.8$ earthquakes from the East African Rift Valley and the Eastern US (the 2011 Virginia earthquake) to improve coverage, since higher-magnitude events are not observed in these regions. Initial CMT solutions were selected from the global CMT catalogue.

We reinverted all source mechanisms in our 3-D starting model using the approach introduced by Liu *et al.* (2004). Source Fréchet derivatives and 100 min seismograms are calculated based on the spectral-element solver SPECFEM3D_GLOBE (Komatsch & Tromp 2002a,b), and waveform measurements of body and surface waves are tailored to FLEXWIN (Maggi *et al.* 2009) window selections. We computed Green’s functions for nine source parameters (six moment-tensor components, depth, latitude, and longitude) in the starting model. When the structural model has changed significantly, this source inversion process may be repeated. Alternatively, source and structural parameters may be determined jointly in iterative adjoint inversions (e.g. Kim *et al.* 2011), but since the computational requirements are more-or-less the same, we preferred inverting for source and structural parameters separately.

The results of the source inversions are summarized in Figs 1(B)–(D). The scalar moment, M_0 , typically changes by less than 30 per cent, with an overall tendency for a reduction compared to the initial CMT solution. Hypocentres generally change by less than 10 km, with a typical shallowing of ridge events. These changes are most likely due to the inclusion of a 3-D crustal model in our source inversions, and are consistent with experiments conducted by Hjorleifsdóttir & Ekström (2010).

4 INVERSION STRATEGY AND WORKFLOW

This study is a first attempt at global FWI. The nomenclature FWI means different things in different areas of seismology. We define FWI as follows:

- (i) Forward simulations and Fréchet derivatives are computed in fully 3-D models.
- (ii) Anelasticity is fully accommodated in all numerical simulations.
- (iii) Phase and amplitude information from three-component seismograms is assimilated.
- (iv) Crust and mantle are updated simultaneously, thereby avoiding any ‘crustal corrections’.

With the exception of using amplitude information our global adjoint tomography may be considered global FWI. Although it is straightforward to include amplitude information in the inversion process, amplitude anomalies are affected by a host of factors and notoriously nonlinear, which is why we chose to initially focus on phase information. At a later stage, we plan to revisit amplitude anomalies and consider lateral variations in attenuation, as Zhu *et al.* (2013) did on a continental scale.

Additionally, rather than blindly assimilating complete seismograms, we use the window selection tool FLEXWIN (Maggi *et al.* 2009) to identify windows in which observed and simulated seismograms are sufficiently close to make a measurement, and to maximize information from our phase measurements, as discussed in

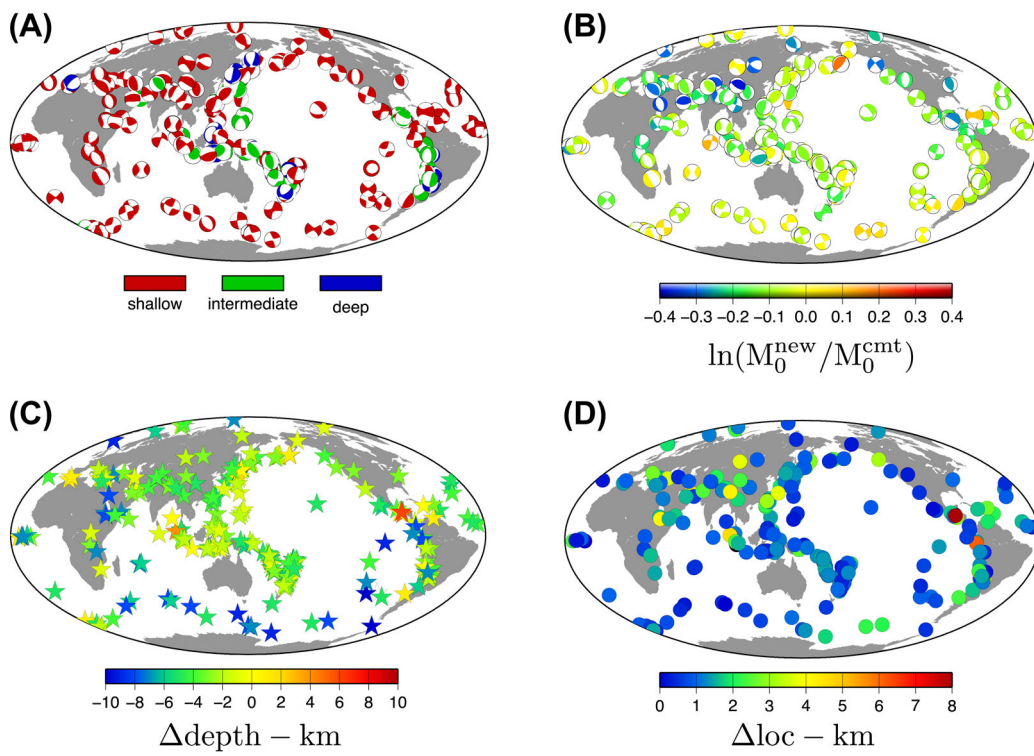


Figure 1. Summary of source inversions for the 253 globally distributed earthquakes used in the structural inversions. Moment magnitudes vary between 5.8 and 7. (A) Focal mechanisms of the selected CMT events. Shallow (<50 km), intermediate depth (50–300 km) and deep (>300 km) events are shown by red, green and blue beach balls, respectively. (B) Focal mechanisms and relative change in scalar moment, $\ln(M_0^{\text{new}} / M_0^{\text{cmt}})$. The scalar moment changes generally less than 30 per cent, and tends to decrease. (C) Change in depth, $\Delta\text{depth} = \text{depth}^{\text{new}} - \text{depth}^{\text{cmt}}$ (in kilometres). Shallow events tend to exhibit the largest depth changes, highlighting the influence of the 3-D crust on source parameters. (D) Change in epicentre, $\Delta\text{loc} = \text{loc}^{\text{new}} - \text{loc}^{\text{cmt}}$ (in kilometres), which is generally less than 5 km.

detail in Section 4.3.1. As the inversion proceeds and the model improves the fit to the data, the number of windows grows, ultimately resulting in the assimilation of complete seismograms.

The inversion strategy in adjoint tomography and FWI is an active area of research. It involves choices with regards to the model (e.g. basis functions, model parametrization, etc.), the data (e.g. period bands, misfit measures, etc.), and the optimization strategy (e.g. regularization, optimization algorithm, etc.), all of which have a direct impact on the final model (e.g. Modrak & Tromp 2016). Once these choices have been made, adjoint inversions are described by a well-defined iterative workflow in which each step may be independently improved for better performance and resolution by adding new capabilities and options. The adjoint tomography workflow consists of four major stages: (1) forward simulations in the current model, (2) pre-processing and construction of adjoint sources, (3) gradient calculation in the current model, and (4) post-processing and model update (Fig. 2). The ultimate goal is to automate the entire workflow by reducing human interaction as much as possible (e.g. Lefebvre *et al.* 2014; Krischer *et al.* 2015a). This has been the approach in industrial FWI problems, where tens to hundreds of iterations are performed, which is possible partly due to relatively better data quality and ray coverage. Our global adjoint tomography workflow is complex and involves a significant number of steps. User interaction is error-prone, especially when performing repetitive tasks. In order to stabilize the entire process, we are currently experimenting with workflow management systems, such as Pegasus (pegasus.isi.edu) (Deelman *et al.* 2015) and RADICAL-Pilot (Merzky *et al.* 2016).

In the following sections, we explain our workflow and FWI strategy in more detail.

4.1 Model basis functions and parametrization

In global tomography it is common to use spherical and cubic splines (e.g. Ritsema *et al.* 1999; Boschi & Ekström 2002; Lebedev *et al.* 2005; Kustowski *et al.* 2008; Ritsema *et al.* 2011), local cells (e.g. Zhou 1996; van der Hilst *et al.* 1997; Kennett *et al.* 1998) or triangular grid points (e.g. Zhou *et al.* 2006). We prefer to use the numerical integration points used in the spectral-element method, that is, the Gauss–Lobatto–Legendre (GLL) points, and smooth the model at a later stage, if need be, rather than projecting it on a smooth basis at the stage of the kernel calculation to minimize possible effects of parametrization on final models (e.g. Trampert & Snieder 1996).

We use a transversely isotropic model parametrization confined to the upper mantle, starting below the Moho. Transverse isotropy is described by five Love parameters, namely, A , C , L , N and F (Love 1927). By introducing the mass density, ρ , transverse isotropy may alternatively be specified in terms of the speeds of vertically and horizontally polarized P waves, α_v and α_h , the speeds of horizontally travelling and vertically or horizontally polarized S waves, β_v (or V_{sv}) and β_h (or V_{sh}), and the dimensionless parameter η . To reduce the dependency of P and S wave-speed models on each other through the shear modulus, we use the bulk sound speed, c , which depends on the bulk modulus, κ . Thus, we are left with five parameters, namely, density, ρ , bulk sound speed $c = \sqrt{\kappa/\rho}$, vertically and

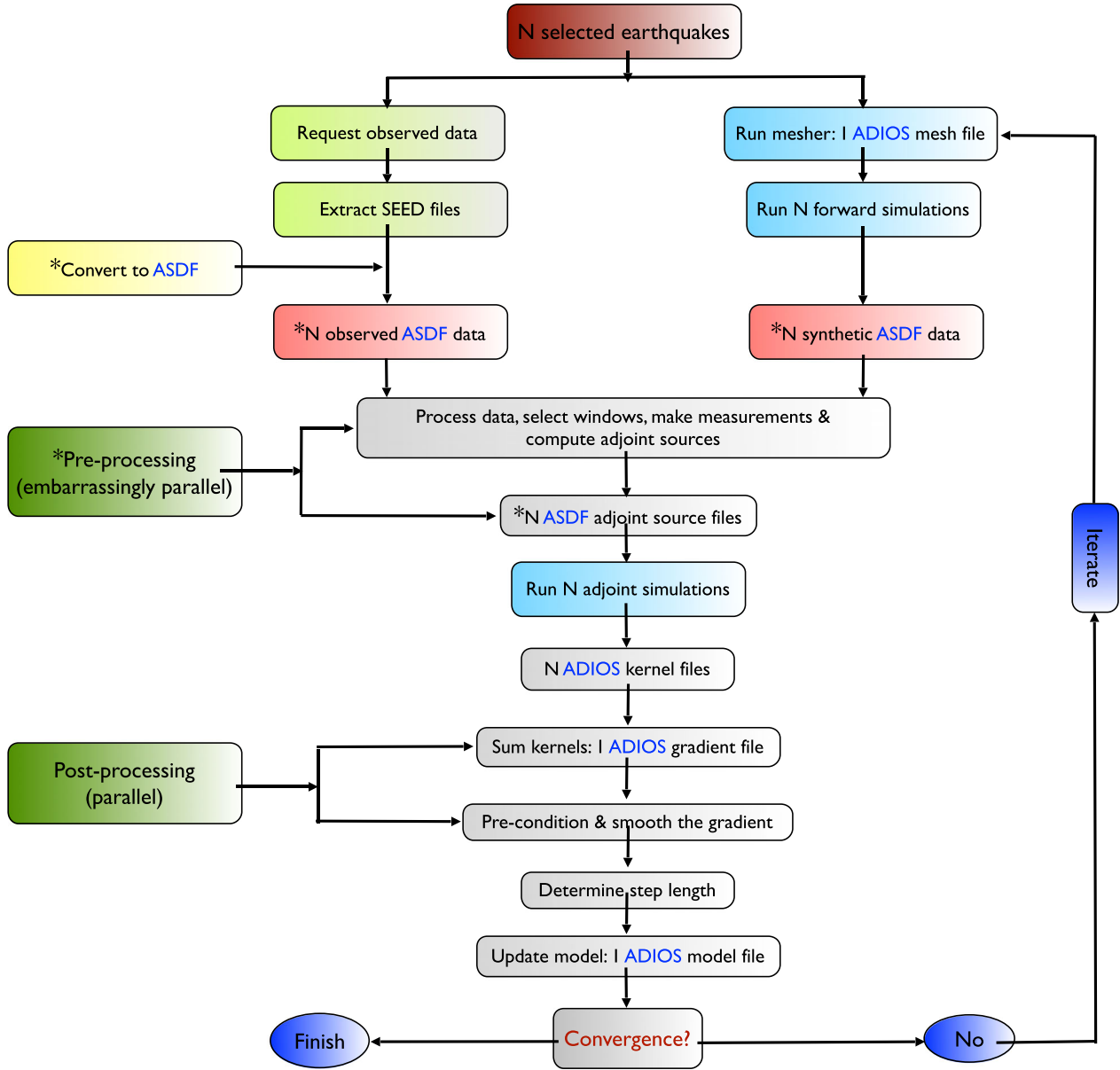


Figure 2. Adjoint tomography workflow. We use the Adaptable I/O System (ADIOS; Liu *et al.* 2014) for fast I/O of computational data, namely, meshes, models, and kernels, and for post-processing. *The Adaptable Seismic Data Format (ASDF; Krischer *et al.* 2016) and the related pre-processing tools were not used in the current inversion, but will be used in future iterations.

horizontally polarized shear wave speeds $\beta_v = \sqrt{L/\rho}$ and $\beta_h = \sqrt{N/\rho}$, and the dimensionless parameter $\eta = F/(A - 2L)$.

Density is generally difficult to constrain within the period range of this study. Therefore, to further simplify the model parametrization, we follow classical global tomographic studies and scale density to shear wave speed via the relation (Montagner & Anderson 1989)

$$\delta \ln \rho = 0.33 \delta \ln \beta, \quad (1)$$

where β is the Voigt average (Babuška & Cara 1991):

$$\beta = \sqrt{\frac{2\beta_v^2 + \beta_h^2}{3}}. \quad (2)$$

This further reduces the number of unknown parameters from five to four, and the gradient of the misfit function, $\delta \chi$, may be expressed as

$$\delta \chi = \int_V K_c \delta \ln c + K_{\beta_v} \delta \ln \beta_v + K_{\beta_h} \delta \ln \beta_h + K_\eta \delta \ln \eta \, dV, \quad (3)$$

where K_c , K_{β_v} , K_{β_h} and K_η are the Fréchet derivatives with respect to the four dimensionless model parameters $\delta \ln c$, $\delta \ln \beta_v$, $\delta \ln \beta_h$ and $\delta \ln \eta$. Perturbations may be defined with respect to either 1-D or 3-D models. In our iterative inversion, perturbations are always with respect to the 3-D model from the previous iteration.

4.2 Numerical simulations

Today's hybrid-architecture high-performance computing (HPC) systems employ graphics cards (GPUs—Graphics Processing Unit)

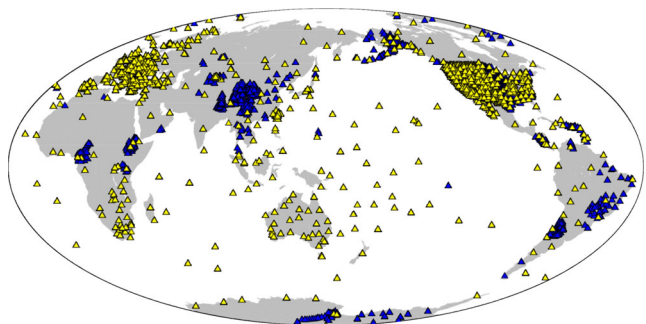


Figure 3. Permanent (yellow) and temporary (blue) stations from the global seismographic network (GSN) and several local arrays, such as USArray, European and Australian networks.

as hardware accelerators connected to the CPU (Central Processing Unit). We used the spectral-element solver SPECFEM3D_GLOBE (Komatitsch & Tromp 2002a,b) accelerated by graphics cards (Komatitsch *et al.* 2010; Komatitsch 2011) for all forward and adjoint simulations. The first twelve iterations were performed with a shortest period of ~ 27 s, and the following three iterations with a shortest period of ~ 17 s. Synthetic seismograms were calculated for the 253 earthquakes shown in Fig. 1(A) recorded by the stations shown in Fig. 3.

In the following, we describe how we combined observed and simulated data to update models.

4.2.1 Forward simulations

3-D forward simulations incorporate the effects of self-gravitation (in the Cowling approximation) (Cowling 1941), rotation, attenuation, ellipticity, the ocean load, and topography & bathymetry, as discussed in Komatitsch & Tromp (2002b). We currently use the 1-D Q model from PREM (Dziewoński & Anderson 1981), which is fixed during the inversion. In the future, when we also assimilate amplitude measurements, we plan to attempt an inversion for lateral variations in attenuation.

For the first nine iterations, we calculated 100 min-long seismograms, containing minor-arc surface waves (G1 & R1) at all epicentral distances. In subsequent iterations, after incorporating the full effects of attenuation (Komatitsch *et al.* 2016) during the calculation of Fréchet derivatives (discussed in more detail later), we used 180 min long seismograms, containing full-orbit Love and Rayleigh surface waves as well as body waves. For topography/bathymetry, we usedETOPO4, a 4 min resolution model subsampled and smoothed fromETOPO1 (Amante & Eakins 2009).

4.2.2 Implementation of the crust

Earth's highly heterogeneous crust has a strong influence on seismic waves in general and on surface waves in particular (Montagner & Jobert 1988), but may also significantly affect body-wave traveltimes (Ritsema *et al.* 2009). Joint inversions for the crust and mantle are challenging, and ‘crustal corrections’ of one form or another are ubiquitous. Two commonly used approximations are: (1) crustal effects are smooth enough to be captured by first-order perturbation theory, and (2) Earth's crust is assumed known and fixed in the inversion. Concerns about the former have been raised by Bozdağ & Trampert (2008) and Lekić *et al.* (2010), whereas Ferreira *et al.* (2010) showed that the latter biases inversions for mantle heterogeneity, for example, by introducing transverse isotropy or

azimuthal anisotropy when there is none. Consequently, crustal corrections may strongly affect models of the mantle and core.

To accommodate the crust more accurately, Fichtner *et al.* (2009, 2013) prefer to fit a long-wavelength equivalent of the crustal signal and update the crust separately using a Backus-averaging technique (Backus 1962), and Lekić & Romanowicz (2011) and French & Romanowicz (2014) follow a similar approach (Capdeville & Marigo 2007). The goal of these efforts is to reduce the computational burden of accommodating the effects of the 3-D crust. Our preferred solution is to accept the complications induced by the crust and fully incorporate it in forward simulations and inversions. As described in Tromp *et al.* (2010), the Moho is honoured by the spectral-element mesh if the crust is less than 15 km thick (mainly oceanic crust) and thicker than 35 km (continental crust), and the Moho runs through mesh elements in ocean-continent transitions. This meshing strategy ensures accurate simulations of global surface-wave propagation.

4.2.3 Adjoint simulations: calculation of Fréchet derivatives

Using the adjoint method, Fréchet derivatives are computed based on two numerical simulations: a forward simulation initiated by a regular source, such as an earthquake, and recorded at a receiver, and an adjoint simulation initiated by placing a fictitious source at the location of a regular station and recorded at the location of the regular source (Tarantola 1984a; Tromp *et al.* 2005). Since the Green's functions are the same in both numerical simulations, if one can simulate the regular forward wavefield, the adjoint wavefield can be simulated in the same fashion by simply changing the source term. The adjoint source term is directly dependent on the chosen misfit function (e.g. Tromp *et al.* 2005; Bozdağ *et al.* 2011), such that the resulting Fréchet derivative, or sensitivity kernel, reflects the measurement.

The biggest challenge in gradient calculations used to be taking into account full attenuation, because the time-reversed reconstruction of the forward wavefield during the convolution with the adjoint wavefield is numerically unstable in the presence of dissipation, as described in detail in Liu & Tromp (2006). Based on a comparison with normal-mode calculations, Zhou *et al.* (2011) showed that for body waves and long-period surface waves physical dispersion is the most important aspect of attenuation for kernel construction, and this effect can be readily accommodated. This was our strategy for the first eight iterations, up to which point we only assimilated minor-arc surface waves with periods longer than 50 s. Indeed, this is a valid approximation at long periods and short epicentral distances, which may safely be used in continental- and regional-scale studies (e.g. Tape *et al.* 2009; Zhu *et al.* 2012; Chen *et al.* 2015). However, at the global scale, especially with the use of major-arc waves at longer epicentral distances and shorter periods ($T < 50$ s), the approximation may no longer be valid. After the stable implementation of full attenuation in adjoint simulations (Komatitsch *et al.* 2016), we switched to exact anelastic kernel calculations after the ninth iteration, and we immediately observed a major benefit for the Love-wave misfit reduction.

In an independent theoretical study, Valentine & Trampert (2016) reported that combining exact wave simulations with approximate kernels may generate larger errors in imaging than a fully asymptotic or approximate approach in both forward and kernel computations. Based on our observations, as we go down to shorter periods, any approximations in wave and kernel simulations should be avoided.

4.3 Pre-processing

We selected data for the 253 earthquakes shown in Fig. 1(A) from the Global Seismographic Network (GSN) and several local continental arrays, such as USArray, and European, Japanese, and Australian networks (Fig. 3). Data are freely available from data centres operated by IRIS (USA) and ORFEUS (Europe). The pre-processing phase of the adjoint tomography workflow involves data culling, time-series analysis, window selection, making measurements, and adjoint source construction (Fig. 2).

4.3.1 Measurement strategy

To avoid nonlinearities, which may occur in FWIs, we used only phase information—targeting elastic structure in the first-generation model—and defined appropriate period bands for measurements at each iteration.

All measurements were made on three-component (vertical, radial, transverse) seismograms, assimilating both body and surface waves. In relatively short time windows, for example, for body waves, we make cross-correlation traveltime measurements, and in sufficiently long time windows, for example, for surface waves, we make frequency-dependent (multitaper) traveltime measurements. The measurements are divided into a number of categories. For example, for our four final period bands on three components we have twelve measurement categories (Fig. 4). The frequency-dependent traveltime misfit in category c may be expressed as

$$\chi_c = \frac{1}{N_c} \sum_{e=1}^E \sum_{i=1}^{N_c^s} \int w_i(\omega) \left[\frac{\Delta\tau_i(\omega)}{\sigma_i} \right]^2 d\omega / \int w_i(\omega) d\omega, \quad (4)$$

where $\Delta\tau_i$ denotes the traveltime anomaly in frequency window w_i , σ_i the associated standard deviation, N_c^s the number of measurements in category c for earthquake e , E the total number of earthquakes, and $N_c = \sum_{e=1}^E N_c^s$ the total number of measurements in category c . If the time window is too short to make a multitaper measurement, we use a cross-correlation measurement instead. The total misfit in all C categories is

$$\chi_{\text{total}} = \frac{1}{C} \sum_{c=1}^C \chi_c. \quad (5)$$

We selected our period bands as follows:

(i) *1st to 5th iteration*: We initiated iterations with 100 min-long seismograms with ~ 27 s resolution, using two period bands, namely, 30–60 s for body waves and 60–120 s for surface waves and long-period body waves. Our strategy was to decrease the lower corner of the surface-wave pass band gradually, as the overall misfit improved.

(ii) *6th to 8th iteration*: We added a 96–250 s long-period surface-wave band. We adjusted the other two period bands to 30–66 s and 56–110 s, respectively, with ~ 10 per cent overlap between bands.

(iii) *9th to 11th iteration*: We incorporated full attenuation in gradient calculations and started using 180 min-long seismograms, thereby incorporating major-arc waves. The period bands were adjusted to 30–59 s, 50–106 s and 90–250 s, respectively.

(iv) *12th to 15th iteration*: We increased the resolution of our simulations by interpolating and resampling our 11th-iteration model from 160 surface elements along each side of the cubed sphere (Komatitsch & Tromp 2002a) to 256 surface elements, thereby reducing the shortest period from ~ 27 s to ~ 17 s. This allowed us to add one more shorter-period body-wave measurement cate-

gory. Thus, we performed the last four iterations with four period bands, namely, 17–38 s for shorter-period body waves, 30–56 s for intermediate-period body waves, 45–110 s for surface waves & long-period body waves, and 92–250 s for long-period surface waves. Note that we used any selected phase in the 45–110 s period band, including minor-and major-arc surface and body waves, whereas we used only body waves in the 17–38 s and 30–56 s period bands, and only surface waves in the 92–250 s period band.

In Fig. 4, our last four period bands together with FLEXWIN window selections are illustrated for a path across the Indian Ocean. We initiated our inversion with about ~ 1.2 million measurements, and gradually increased this number to ~ 2.6 million after the 9th iteration, culminating in the assimilation of more than 3.8 million measurements during the last four iterations.

4.3.2 Challenges of data pre-processing on large HPC systems

While several different groups have their own data formats, Seismic Analysis Code (SAC; Helffrich *et al.* 2013) has been the standard data format in earthquake seismology. However, handling data in SAC format during pre-processing involves millions of files, and the related I/O traffic can cripple the file system. This is undesirable on high-performance clusters, and highlights the need for a new seismic data format which satisfies the needs of modern seismology. For this reason, a new Adaptable Seismic Data Format (ASDF) is being developed (Krischer *et al.* 2016). ASDF is based on HDF5 and combines all seismic traces for an event in a single file. Thus, one needs only two files per event, one for observed data and one for synthetic data. Additionally and importantly, ASDF enables users to keep track of data provenance, which is stored with the data in the same container. We are in the process of migrating the entire pre-processing phase to a Python-based workflow which seamlessly integrates ASDF with ObsPy (Krischer *et al.* 2015b), a Python framework for processing seismological data. As part of this migration, Python versions of FLEXWIN (pyflex) and the measurement code (pyadj) are being developed.

4.4 Post-processing

Once the gradient calculations for all earthquakes are completed, the adjoint tomography workflow continues with a post-processing phase leading to a model update (Fig. 2). The post-processing phase uses the Adaptable I/O System (ADIOS) (Liu *et al.* 2014) developed by Oak Ridge National Laboratory for fast parallel I/O, which also greatly reduces the number of files. The post-processing steps leading to the model update are summarized in the next sections.

4.4.1 Summation of event kernels

Adjoint simulations result in event kernels for each earthquake, which are summed to obtain the full gradient of the misfit function. This summation is performed at the GLL level.

4.4.2 Smoothing the gradient

Smoothing serves the same purpose as damping in classical tomography and is applied for the following reasons: (1) The gradient is a result of numerical simulations and should be smoothed to reflect the numerical resolution. (2) Smoothing should be applied to balance imperfect ray coverage, which is an issue for global

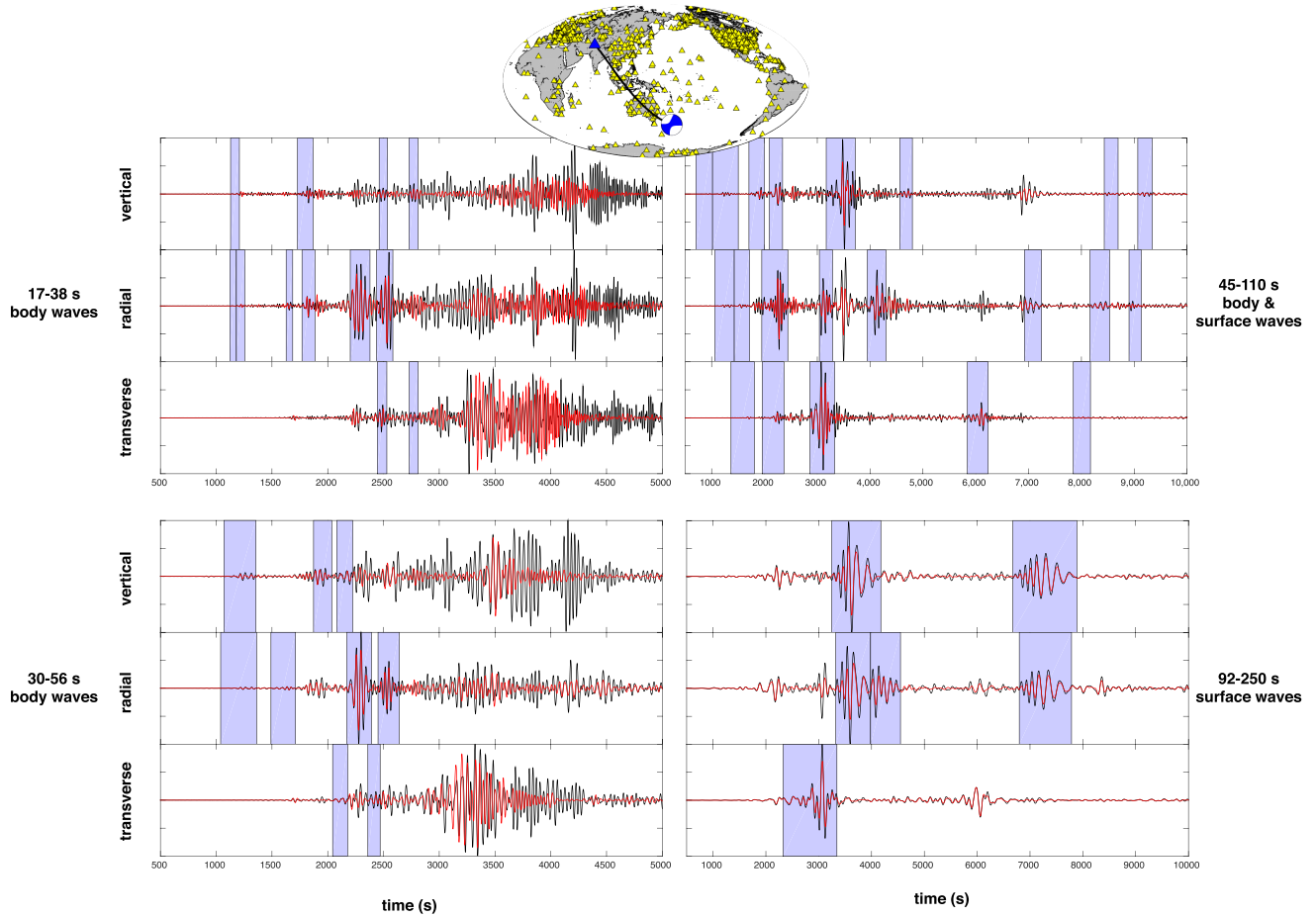


Figure 4. Sample window selections by FLEXWIN (Maggi *et al.* 2009; blue windows) showing the period bands used during the last three iterations. Shown are vertical, radial, and transverse component records of observed (black) and synthetic (red) seismograms of the 2010 September 3 New Zealand earthquake ($M_w = 7$, depth = 12 km) recorded at station KBL in Kabul, Afghanistan.

studies. We used a Gaussian smoothing operator similar to the one described in Zhu *et al.* (2015), such that the gradient is smoothed by a 3-D Gaussian in the lateral and radial directions with suitably chosen half-widths. The amount of smoothing is defined as a function of ‘ray (kernel) density’, which is calculated based on the pseudo-Hessian kernel discussed in the next section. This leads to a multiscale smoothing of gradients, thereby enabling us to resolve smaller-scale heterogeneities underneath locations with dense station coverage, for example North America, Asia and Western Europe. A typical example of global ray (kernel) coverage is shown in Fig. 5, illustrating that coverage significantly decreases from the upper mantle into the lower mantle, and from the Northern Hemisphere into the Southern Hemisphere. The worst coverage is in the lower mantle of the Southern Hemisphere, and the best coverage is in the upper mantle beneath North America, thanks to USArray.

4.4.3 Pre-conditioning

Following Luo *et al.* (2013), we used a pre-conditioner based on the interaction between the forward and adjoint accelerations, namely the pseudo-Hessian

$$P(\mathbf{x}) = \sum_{e=1}^E \int \partial_t^2 \mathbf{s}(\mathbf{x}, t) \cdot \partial_t^2 \mathbf{s}^\dagger(\mathbf{x}, T-t) dt. \quad (6)$$

Here \mathbf{s} and \mathbf{s}^\dagger denote the forward and adjoint displacements, respectively, and E denotes the number of earthquakes. This preconditioner corresponds to the diagonal terms of the Hessian. These diagonal terms mimic ray (kernel) coverage, and thus this preconditioner not only suppresses high amplitudes around sources and receivers, but also balances imperfect coverage.

4.4.4 Optimization

We performed all iterations based on a conjugate-gradient method (Fletcher & Reeves 1964). Following Tromp *et al.* (2005), Tape *et al.* (2010) and Zhu *et al.* (2012), we determined the search direction via

$$\mathbf{d}_i = -\mathbf{g}_i + \beta \mathbf{d}_{i-1}, \quad (7)$$

where \mathbf{g} and \mathbf{d} are the gradient and search direction from the current and previous iterations, respectively, and β is given by

$$\beta = \frac{\mathbf{g}_i^T \cdot (\mathbf{g}_i - \mathbf{g}_{i-1})}{\mathbf{g}_{i-1}^T \cdot \mathbf{g}_i}. \quad (8)$$

Although some studies show that conjugate gradient and quasi-Newton methods give similar convergence rates during the first few iterations (e.g. Luo *et al.* 2013), we are planning to switch to the L-BFGS method (Nocedal 1980) in future iterations, which may help with imperfect ray (kernel) coverage.

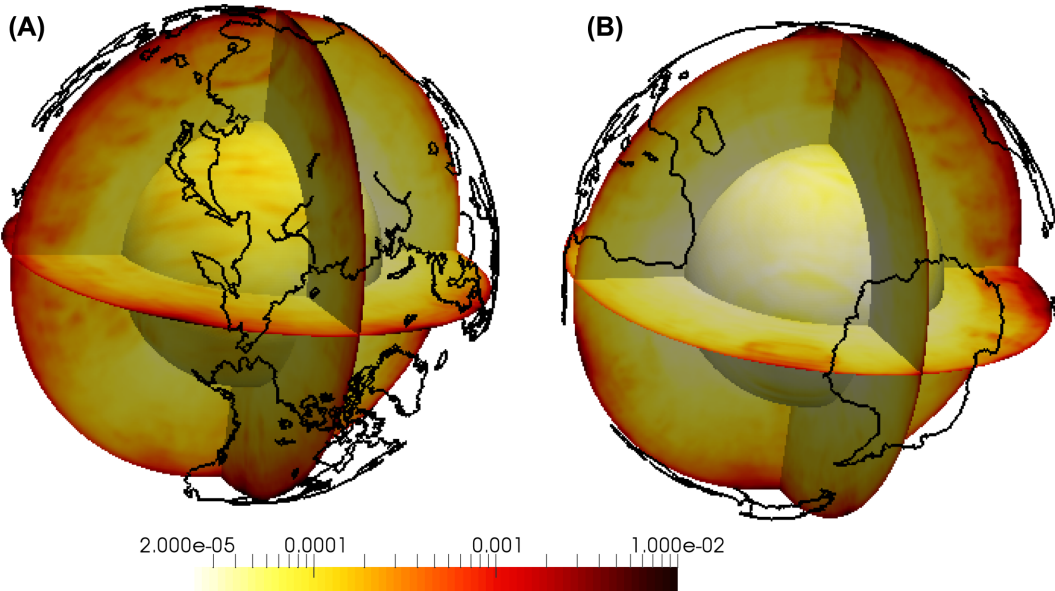


Figure 5. Pseudo-Hessian kernel defined by eq. (6) calculated based on the measurements for the final model to illustrate global ray (kernel) coverage. (A) Northern Hemisphere, (B) Southern Hemisphere. Minimum and maximum values denote areas with poor and good coverage, respectively. The pseudo-Hessian is used to determine the amount of smoothing of the gradient, as well as a pre-conditioner.

4.4.5 Determining the step length

Once we establish the search direction, we use a line search to determine the step length for the model update, as described in Tape *et al.* (2007). Following Zhu *et al.* (2015), we run forward simulations for a subset of 24 earthquakes for various step lengths. In global inversions, we generally use 0.5–2 per cent perturbations in the search direction. The challenge is to find a step length that satisfies all measurement categories described in Section 4.3.1. Once the step length is determined, the model parameters \mathbf{m} may be updated via

$$\ln \frac{\mathbf{m}_{i+1}}{\mathbf{m}_i} = \alpha \mathbf{d}_i, \quad (9)$$

Table 1. Core hours spent during the source inversions and 15 structural iterations. The CPU version of SPECFEM3D_GLOBE was used for the source inversions and the GPU version was used for all 15 iterations. Note that CPU core hours listed for Structural Inversions–I are provided for comparison with the GPU version, using the same number of GPUs as CPUs. Full attenuation in adjoint simulations was used after the eight iteration (Structural Inversions–II), when the record length was increased to 180 min. Resolution was increased by going down to a minimum period of 17 s during the last three iterations (Structural Inversions–III).

Source inversions	1 event	253 events	
CPU-h, $T_{\min} \sim 27$ s 100 min seismograms	~7500 h	~1.9M h	
Structural Inversions–I			
CPU-h, $T_{\min} \sim 27$ s 100 min seismograms (kernels with physical dispersion)	1 event ~750 h (forward) + ~2250 h (adjoint)	1 iteration (253 events) ~760 000 h	8 iterations ~6M h
GPU-h, $T_{\min} \sim 27$ s 100 min seismograms (kernels with physical dispersion)	~12.5 h (forward) + ~38 h (adjoint)	~12 650 h	~100 000 h
Structural Inversions–II			
GPU-h, $T_{\min} \sim 27$ s 180 min seismograms (kernels with full attenuation)	1 event ~22.5 h (forward) + ~60 h (adjoint)	1 iteration (253 events) ~15 200 h	4 iterations ~60 800 h
Structural Inversions–III			
GPU-h, $T_{\min} \sim 17$ s 180 min seismograms (kernels with full attenuation)	1 event ~58 h (forward) + ~150 h (adjoint)	1 iteration (253 events) ~52 600 h	3 iterations ~158 000 h

where α and \mathbf{d}_i are the step length and the search direction from the i th iteration, respectively.

4.5 Computational requirements

All numerical simulations were performed in parallel with the spectral-element seismic wave propagation solver SPECFEM3D_GLOBE. The computational cost is independent of the number of seismic stations and scales linearly with the number of earthquakes. The computational requirements are summarized in Table 1. We observed longer simulation times during adjoint calculations due to SAC I/O traffic. We expect better performance with ASDF, which is designed to reduce I/O.

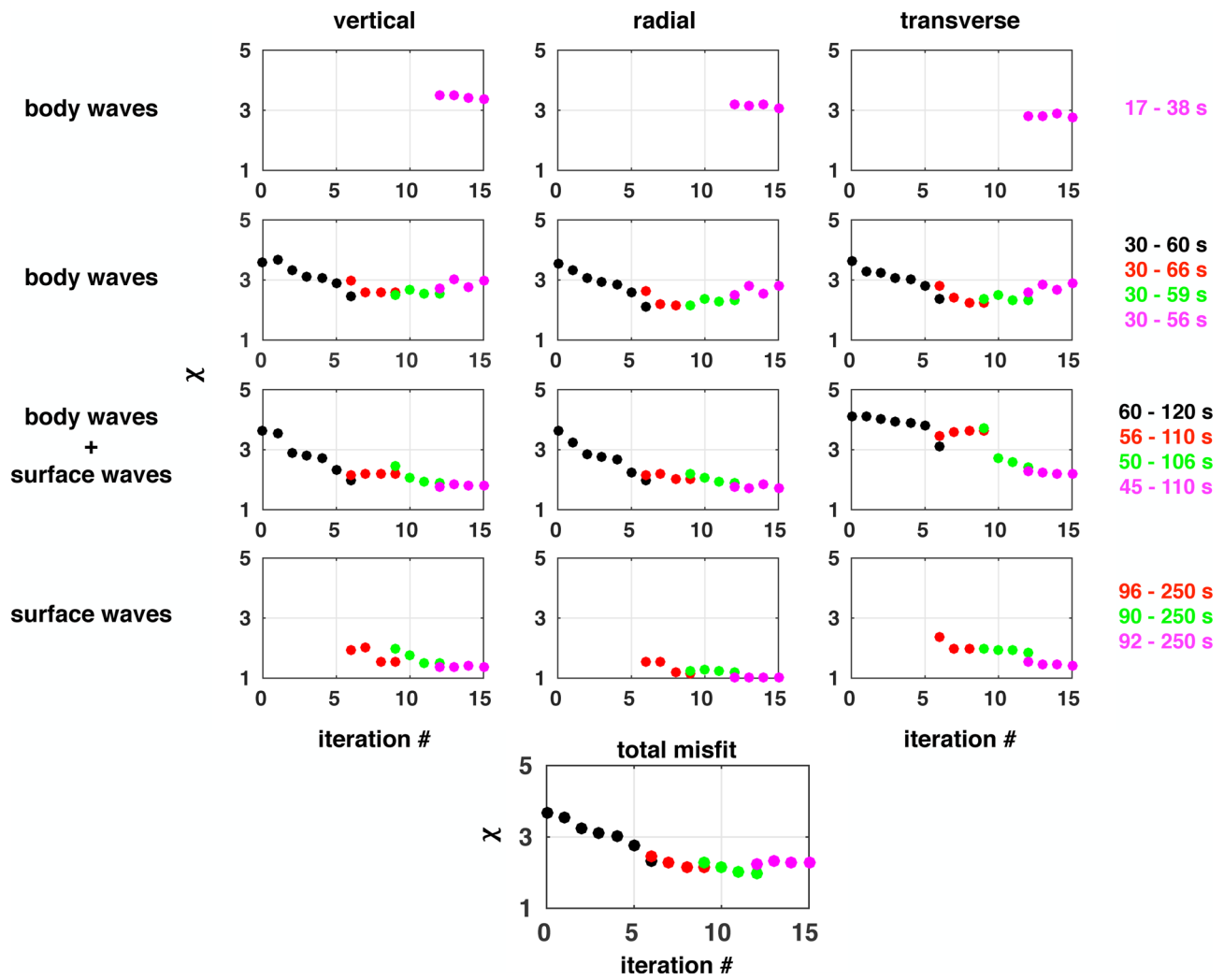


Figure 6. Total misfit reduction (bottom panel) after 15 iterations, and misfit reductions in each measurement category in different period bands (top four rows) on three components (columns). Colours identify various period bands as labelled in the figure. Measurement windows were reselected by FLEXWIN whenever period bands were redefined.

5 FIRST-GENERATION GLOBAL MODEL GLAD-M15

In this section, we present the ‘first generation’ global adjoint tomography model **GLAD-M15** (**G**lobal **A**djoint tomography-**M**odel iteration **15**), which is the result of 15 tomographic iterations.

5.1 Misfit reduction

Fig. 6 summarizes the misfit reduction. The inversion seeks to minimize the total misfit, given by eq. (5), obtained by summing the misfits in each of the sub-categories, given by eq. (4). Thus, we expect the total misfit to be steadily reduced, even though the misfits in each subcategory may not be. Note, however, that the misfit function is a continually moving target, because we seek to increase the number of measurements and gradually broaden the frequency content as the iterations progress. Consequently, when new categories are introduced, the new misfit values are sometimes slightly higher than they were in the previous iteration. The overall misfit reductions in all categories indicate that our gradient is well balanced.

We incorporated the longest-period surface waves ($\sim 90\text{--}250$ s) and shortest-period body waves ($\sim 17\text{--}38$ s) during the 6th and 12th iterations, respectively. Slight jumps in misfits are observed at the 6th, 9th and 12th iterations due to changes in the number of windows and period bands. The overall misfit reduction is smooth and gradual, and flattens towards the 15th iteration, which is an indication of convergence with the current data set within data errors. Note that up to the 9th iteration, body- and surface-wave misfits on the transverse component (Fig. 6, third row, third column) decreased significantly slower than on the other components. This signals the introduction of full attenuation in adjoint simulations, as described in Komatsch *et al.* (2016).

5.2 Traveltime histograms

In Fig. 7, we show multitaper (for dispersive waveforms) and cross-correlation (for non-dispersive waveforms) traveltimes for the final four measurement categories on all three components for starting model S362ANI+Crust2.0 (M00) and final model GLAD-M15 (M15). Note how, unlike the M00 histograms, the M15 histograms are nicely peaked and centred on zero and more Gaussian in shape in all 12 misfit categories.

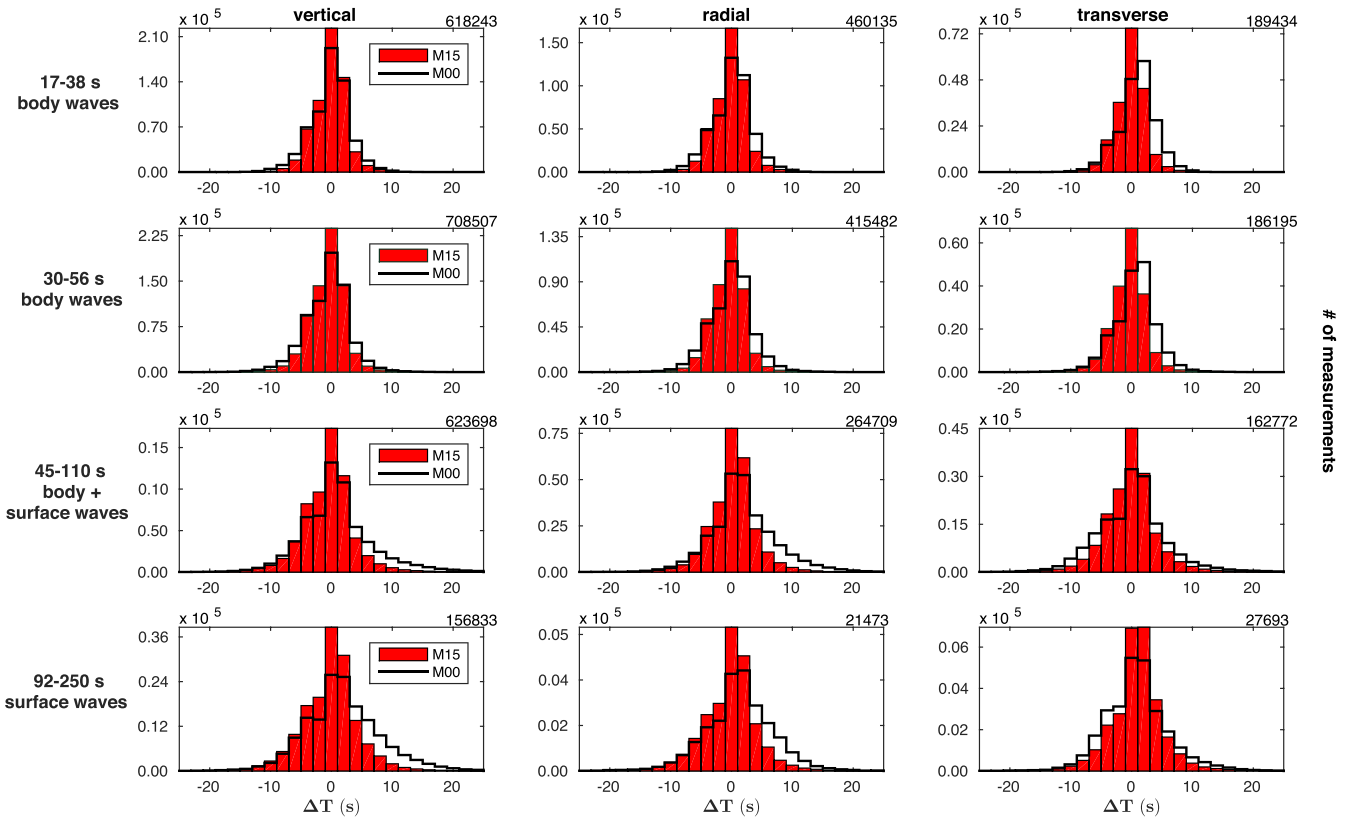


Figure 7. Multitaper (dispersive waves) and cross-correlation (non-dispersive waves) traveltimes histograms for the starting model S362ANI+Crust2.0 (Kustowski *et al.* 2008; Bassin *et al.* 2000) (M00) and the 15th iteration model GLAD-M15 (M15) in the 12 measurement categories used during the last four iterations. The numbers in the top-right of each plot denote the number of measurements in each category. The total number of measurements exceeds 3.8 million.

5.3 Map views

In GLAD-M15, we observe well-known plumes, hotspots, and slabs emerging from smooth starting model S362ANI+Crust2.0, particularly in regions with good ray coverage. Figs 8 and 9 show map views centred on the Pacific and Africa at 250 km depth. Major hotspots and plumes, such as Tahiti, Caroline, Hawaii, Bermuda and Kerguelen, are nicely resolved, as are slabs in the Aleutians, Scotia Arc, Hellenic Arc and Tonga, and collision zones, such as the Himalayas. The changes in our model are non-uniform due to our multismoothing strategy, in which we smooth areas with good coverage less to allow the introduction of smaller-scale features, whereas we smooth areas with relatively poor coverage, such as Africa or the Southern Hemisphere, more. The most pronounced changes occur in the upper mantle, where we have the densest ray coverage (Fig. 5). GLAD-M15 naturally resembles S362ANI at long wavelengths, and remains close to it in areas of poorer coverage.

To better depict differences between our final and starting models, we plot vertically polarized shear-wave-speed perturbations in GLAD-M15 with respect to S362ANI+Crust2.0 in Fig. 10. The major absolute changes (>2 per cent) are in the upper mantle, particularly beneath North America and Europe, thanks to dense seismic networks. Perturbations gradually diminish with depth due to reduced data coverage and our multiscale smoothing strategy. Near the CMB, the absolute changes are within ~0.5 per cent, and the largest perturbations are observed beneath the Pacific. These perturbations are generally larger than in model S362ANI+M (Moulik & Ekström 2014)—a recent updated version of S362ANI with a larger data set that includes normal-mode splitting functions—except near the CMB beneath the Pacific. GLAD-M15 also intro-

duces more localized and higher-resolution features, for example, in subduction zones.

5.4 Notable features: plumes, hotspots and slabs

In this section, we present some of the plume, hotspot, and slab features in GLAD-M15. In Fig. 11, three vertical cross-sections are shown, one along the equator and two along meridians. We observe enhancements of Pacific plumes, hotspots, and subduction zones. We also see enhancement of the African plume, as well as the Caroline and Galapagos hotspots in the Pacific. As shown in the bottom row of Fig. 11, the Pacific plume is enhanced near the CMB. Changes underneath Africa are less dramatic than underneath the Pacific due to poorer sampling. We also observe subducted plates and their remnants in the lower mantle, for example, underneath Asia.

One of the most striking features in GLAD-M15 is the Tahiti plume, as shown in Figs 12(A) and (B). The plume originates at the CMB, gets flattened around 1000 km, which may be associated with a viscosity change (e.g. Rudolph *et al.* 2016), and bends towards Tonga, likely interacting with the slab along the trench (e.g. Chang *et al.* 2016). The Tahiti and Samoa plumes appear to originate from one superplume in the lower mantle, and their continuation in the upper mantle is most pronounced in Vp/Vs ratios. We see a similar enhancement of the Caroline plume, which also flattens at around 1000 km, as supported by Vp/Vs ratios.

In the horizontal sections shown in Fig. 13, most of the North American low-wave-speed zones appear in GLAD-M15, such as Yellowstone, Raton and Anahim, as well as Bowie and Cobb.

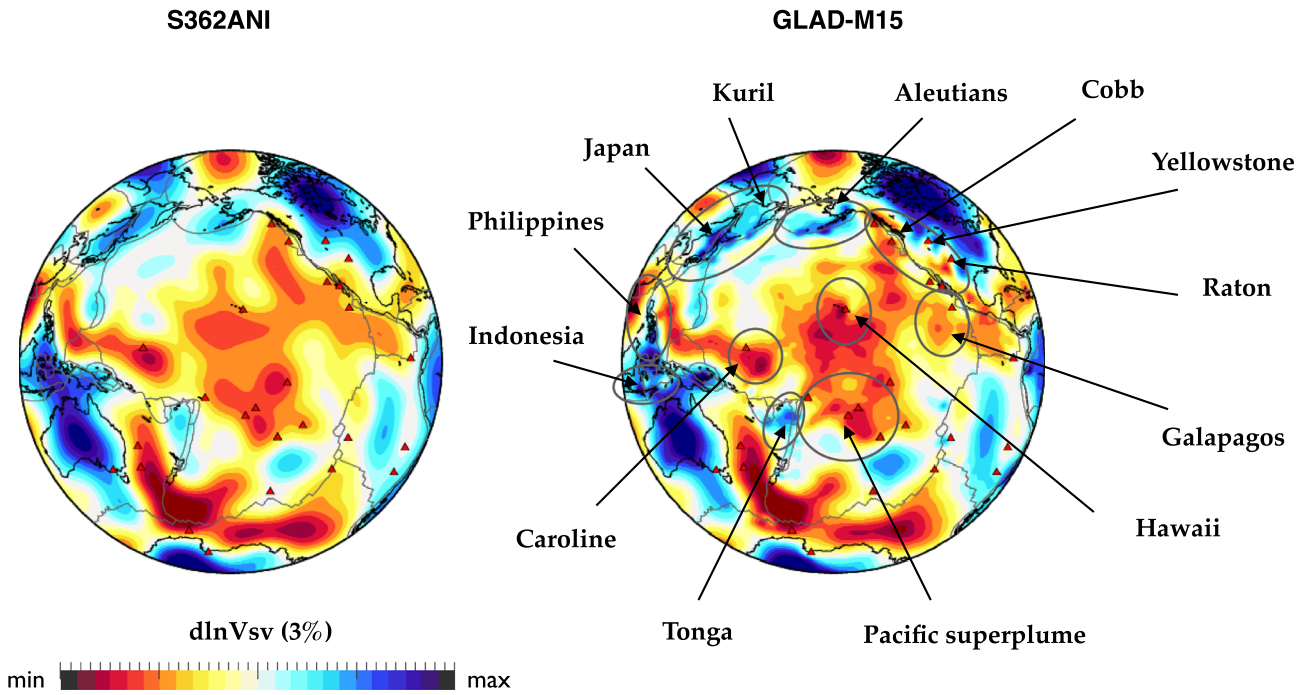


Figure 8. Map views of vertically polarized shear-wave-speed perturbations in starting mantle model S362ANI (left) and GLAD-M15 at 250 km depth. Notable slabs and plumes/hotspots enhanced in GLAD-M15 are marked. Each model is shown with respect to its own mean. Plate boundaries are from Bird (2003).

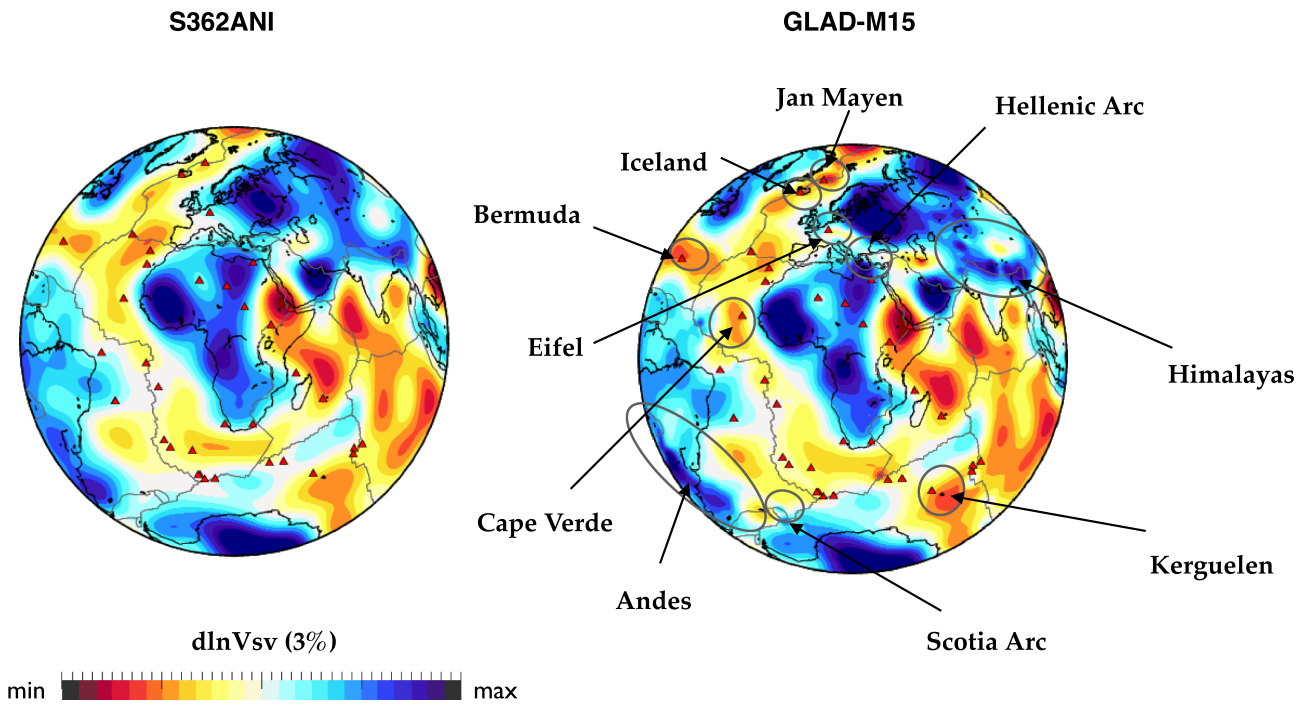


Figure 9. Same as Fig. 8, except centred on Africa.

Yellowstone is currently debated in terms of its size, depth extent and resolution (e.g. Smith & Braile 1994; Pierce & Morgan 2009; Faccenna *et al.* 2010; Fouch 2012). Thus, it is exciting to observe such a local upper mantle feature in a global tomographic model in an area where we have some of the best ray coverage. Furthermore, the slab along the Aleutians has become clearly visible, both in map view and in vertical cross-sections. Yellowstone, Raton, Anahim, and Bowie extend down to the 660-km discontinuity,

as best illustrated in V_p/V_s ratios. Transverse isotropy (TI) underneath Yellowstone and Raton is mainly showing $V_{sh} > V_{sv}$, which is consistent with an interpretation in terms of predominantly horizontal flow in a plume head. Although the resolution of TI may not be perfect, particularly at this scale, we report a clear slab signature in the TI plots with persistent $V_{sh} > V_{sv}$ all around the globe, consistent with predominantly vertical flow (e.g. Montagner 1998). In the lithosphere and asthenosphere, V_{sh} is typically larger than

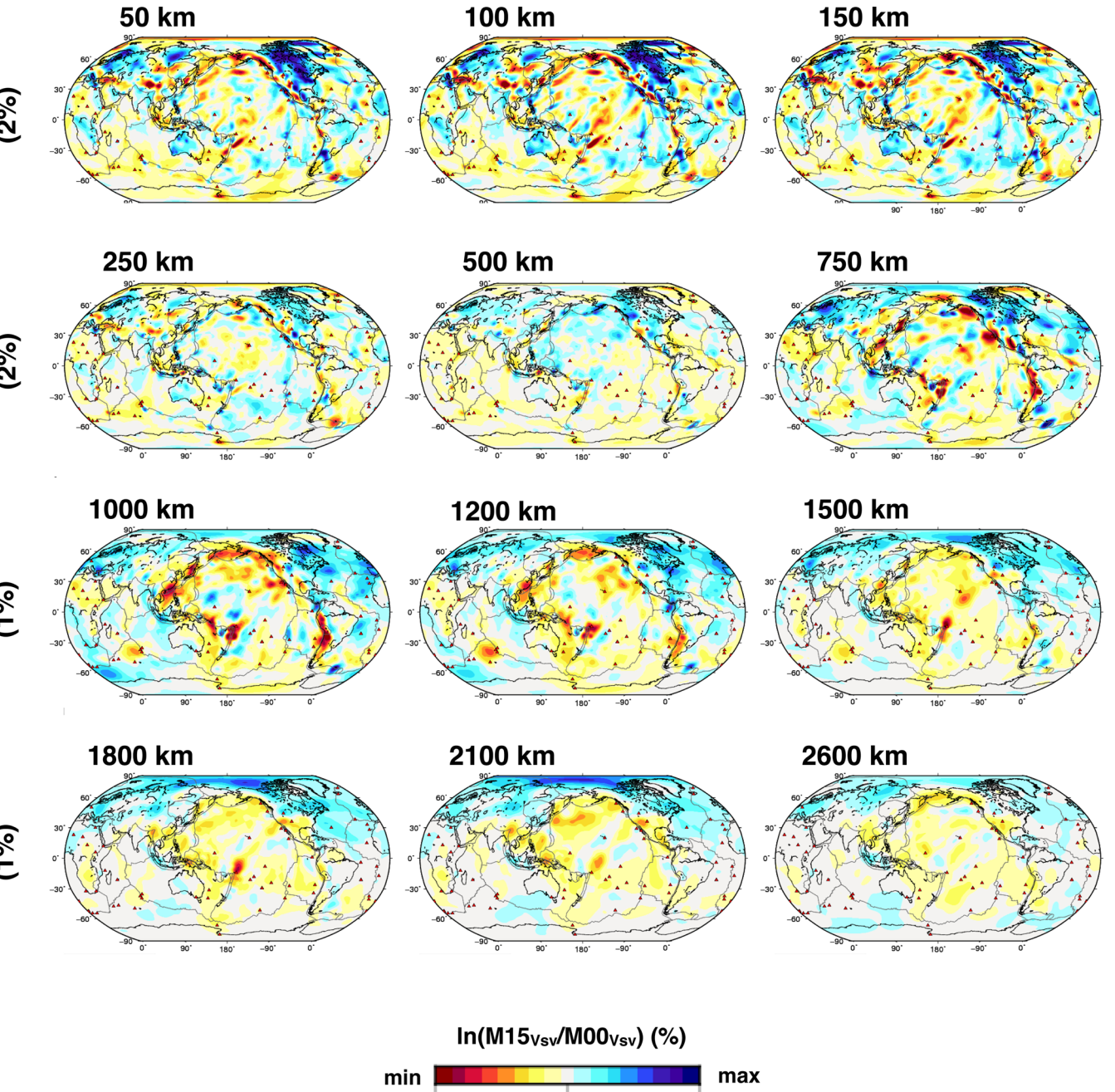


Figure 10. Vertically polarized shear-wave-speed perturbations in GLAD-M15 with respect to S362ANI+Crust2.0, highlighting differences between the 15th iteration model (M15) and the 3-D starting model (M00) ($\ln(M15_{Vsv}/M00_{Vsv})$). Note the changing colour scales, as indicated. Note also that in the rest of this article all shear-wave-speed perturbations are plotted with respect to their own mean.

V_{sv} , consistent with flow/strain-induced horizontal alignment of the olivine fast axis. Subduction of the lithosphere gradually tilts this picture, resulting in V_{sv} being larger than V_{sh} in steeply subducting slabs (e.g. Song & Kawakatsu 2012).

In Fig. 14 we consider Antarctica, with a focus on the Erebus hotspot, a well-known active Antarctic volcano. As previously mentioned, resolution in this part of the globe is challenging due to a paucity of data. Despite this, we clearly observe an enhanced image of the Erebus hotspot, illustrating the power of the methods and tools that we are currently using for imaging. With the help of temporary Antarctic seismic networks (see Fig. 3), we observe thickening of the low-wave-speed structure underneath Erebus, which goes down

to about 1200 km, as supported by V_p/V_s ratios and transverse isotropy characterized by $V_{sh} > V_{sv}$.

Subduction zones are distinctly enhanced in GLAD-M15, for example, in Japan, Izu-Bonin, Marianna, Indonesia and the Aleutians. We also resolve slabs that do not exist in the starting model, such as the Hellenic and Scotia Arcs (Figs 15 and 16). We clearly observe a slab signature in V_p/V_s ratios, with relatively low values, and in V_{sv}/V_{sh} ratios, showing significant transverse isotropy with faster V_{sv} speeds all around the globe. We see a continuation of the Hellenic slab below the 660 km discontinuity, in agreement with previous studies (e.g. Spakman *et al.* 1993; Zhu *et al.* 2012). The Scotia Arc is another challenging location for imaging due to poor

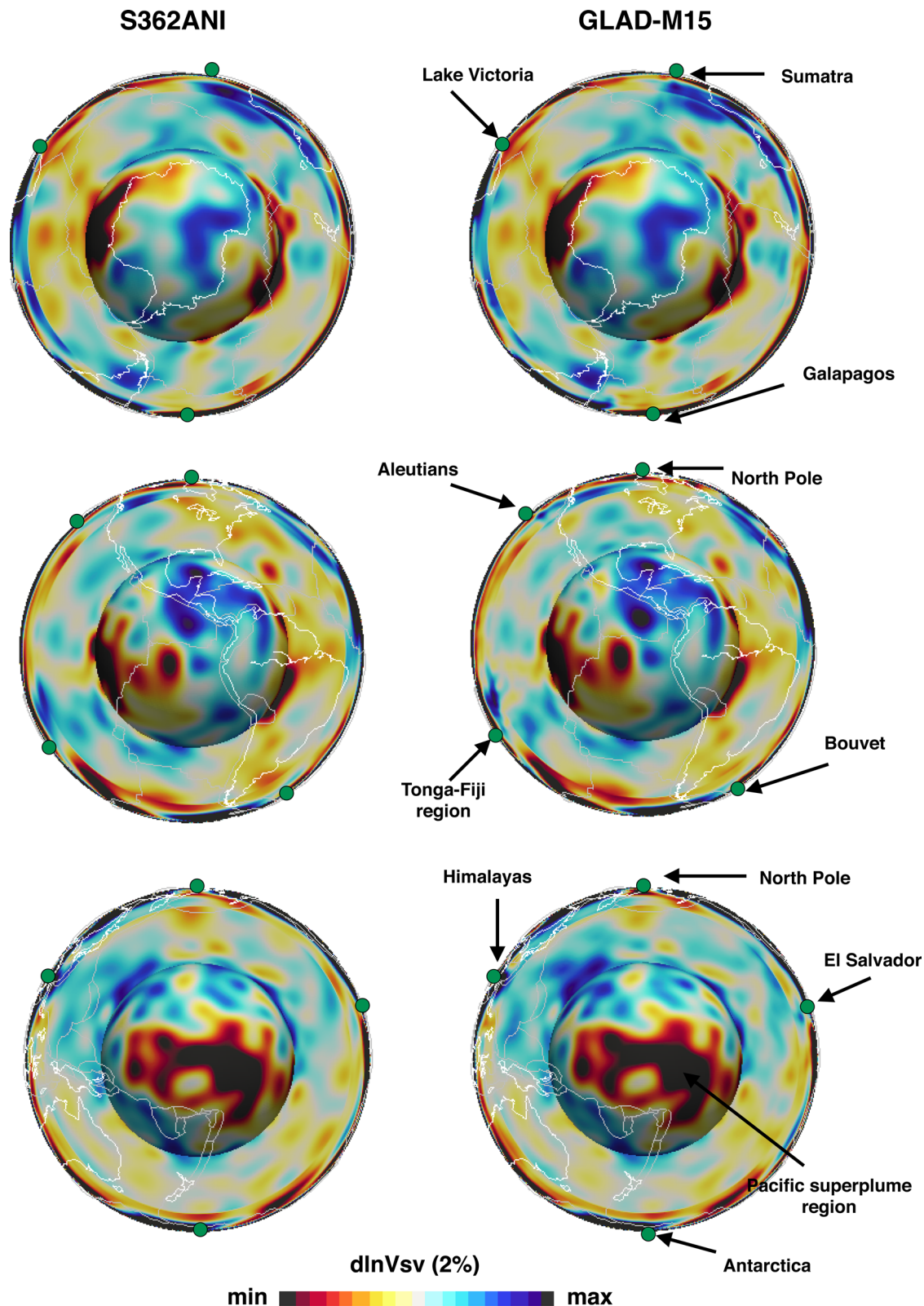


Figure 11. Vertical cross-sections of vertically polarized shear-wave-speed perturbations in starting model S362ANI+Crust2.0 and GLAD-M15 along the equator and in two meridional sections. Map views denote the CMB, and each model is plotted relative to its own radial mean.

ray coverage. Li *et al.* (2008) obtained a *P*-wave slab signature down to ~ 660 km, and it has been argued that the slab likely does not penetrate into the lower mantle (e.g. Loiselet *et al.* 2010). Our images of the Scotia arc are in overall agreement with Li *et al.* (2008),

but we observe stronger perturbations and likely penetration into the lower mantle. Despite being a young slab, lower-mantle penetration is tectonically possible considering its age and the current 69–78 mm yr $^{-1}$ subduction rate (Thomas *et al.* 2003).

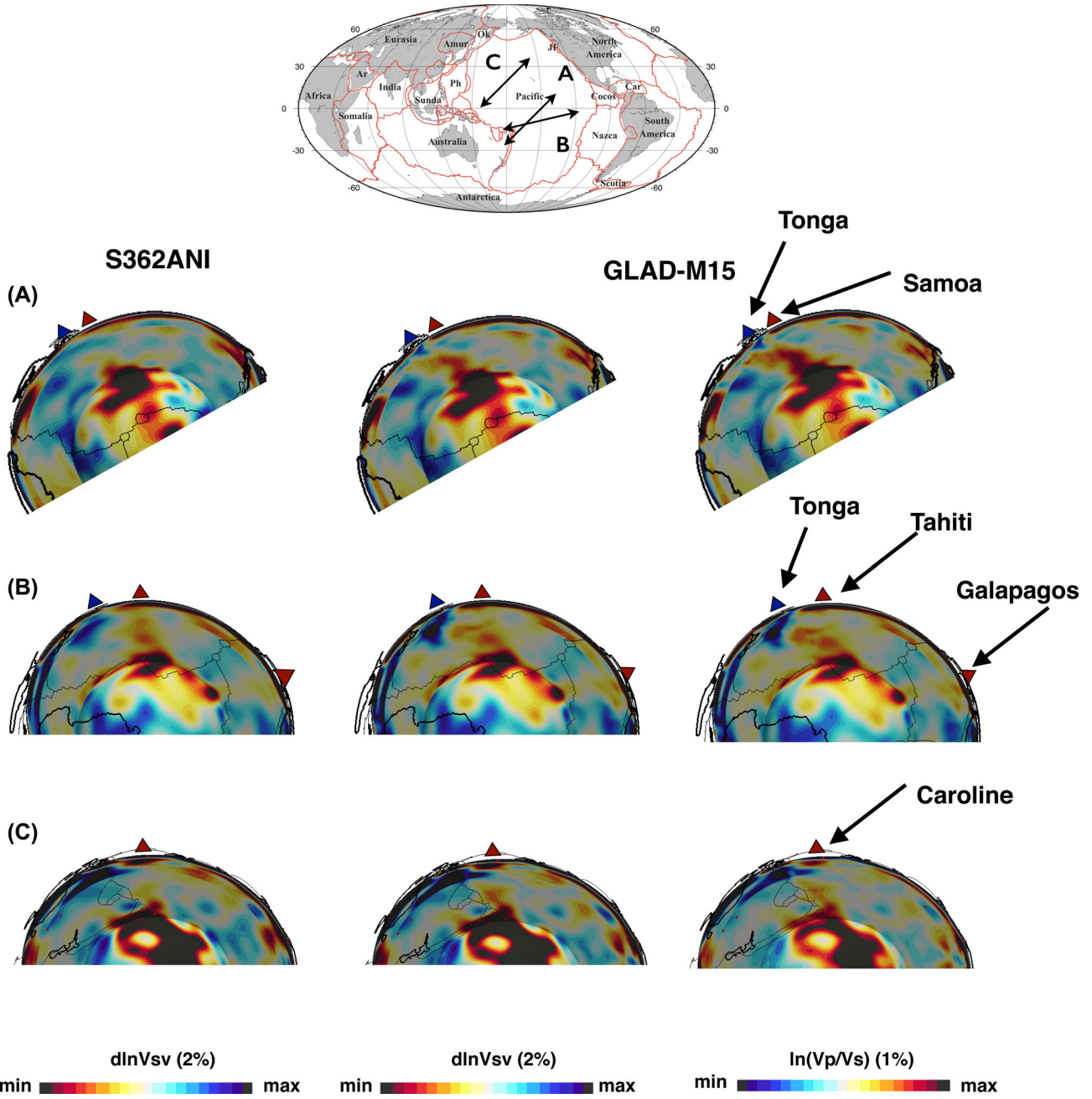


Figure 12. Vertical cross-sections (top map) of vertically polarized shear-wave-speed perturbations in starting model S362ANI+Crust2.0 (first column) and GLAD-M15 (second column) in the Pacific superplume region, showing the Tahiti/Samoa plumes as well as the Caroline plume. The third column shows the Vp/Vs ratio in GLAD-M15. Map views denote the CMB, and each model is plotted relative to its own radial mean.

Comparisons of transverse isotropy and Vp/Vs ratios between GLAD-M15 and S362ANI+Crust2.0 at several depths are shown in Fig. 17. Our large-scale transversely isotropic perturbations in the upper mantle are in overall agreement with model S362ANI+M (Moulik & Ekström 2014) which is an updated version of our starting model S362ANI. However, our perturbations diminish more rapidly below ~ 250 km, which is more consistent with Panning *et al.* (2010) and Chang *et al.* (2014). GLAD-M15 exhibits more localized anomalies around slabs and plumes, and contains features consistent with Chang *et al.* (2014) in the upper mantle beneath the Samoa-Tonga region, which may indicate a slab-plume interaction. Similarly, our Vp/Vs ratios are also in agreement with values determined by Moulik & Ekström (2016), but again reveal sharper anomalies around slabs and plumes.

5.5 Resolution tests

It is common to use checkerboard tests to estimate resolution in tomographic studies, but this is computationally unfeasible for 3-D FWI, particularly on a global scale. Such tests would require the same number of iterations—and hence the same computational resources—as the actual inversion. To ameliorate this problem, Fichtner & Trampert (2011) introduced the ‘point-spread function’ (PSF) test. To perform such a test, a finite-difference approximation is used to calculate the action of the Hessian on a localized model perturbation:

$$\mathbf{H} \cdot \delta\mathbf{m} \approx \mathbf{g}(\mathbf{m} + \delta\mathbf{m}) - \mathbf{g}(\mathbf{m}), \quad (10)$$

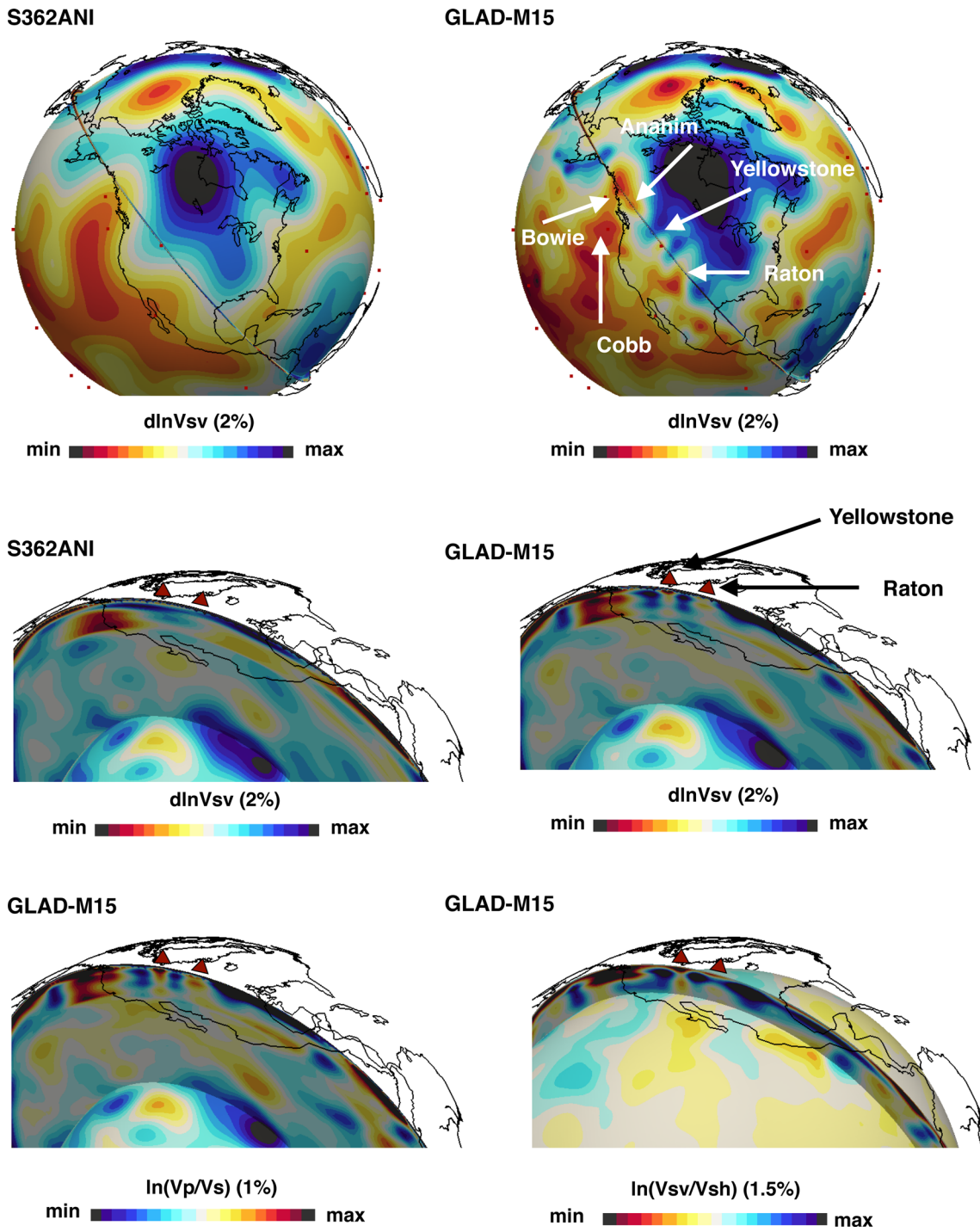


Figure 13. Map views at 250 km depth (top row) and vertical cross-sections (middle row) of vertically polarized shear-wave-speed perturbations in the starting model S362ANI+Crust2.0 and GLAD-M15 underneath North America. Also shown are V_p/V_s ratios (bottom row, left) and transverse isotropy (bottom row, right). Map views in the middle and third row (left) denote the CMB, and the map view in the bottom right panel denotes the 660 km discontinuity, below which transverse isotropy vanishes. Each model is plotted relative to its own radial mean.

where H denotes the Hessian and $\delta\mathbf{m}$ refers to a localized model perturbation with respect to the current model \mathbf{m} . The misfit gradient \mathbf{g} is evaluated for both models \mathbf{m} and $\mathbf{m} + \delta\mathbf{m}$. Based on the action of the Hessian on the model perturbation, $H \cdot \delta\mathbf{m}$, one is able to assess the curvature of the misfit function at a particular ‘point’ in the model space, reflecting the degree of ‘blurring’ of that point. Since we have to calculate the misfit gradient $\mathbf{g}(\mathbf{m} + \delta\mathbf{m})$ for the perturbed model and we already have the gradient $\mathbf{g}(\mathbf{m})$ for the current model, the computational requirements for a single spot

analysis are the same as for one full iteration. Recently, a stochastic extension to this approach has been proposed by Fichtner & van Leeuwen (2015) based on random probing of the Hessian and of the model parameters. In this approach the resolution length of each parameter of interest may be obtained with roughly 5 iterations. We intend to consider such tests in the future.

We selected two specific locations for PSF tests, namely, Yellowstone and Erebus. We perturbed the 14th-iteration model by a spherical Gaussian with a size close to the hotspot of interest, and

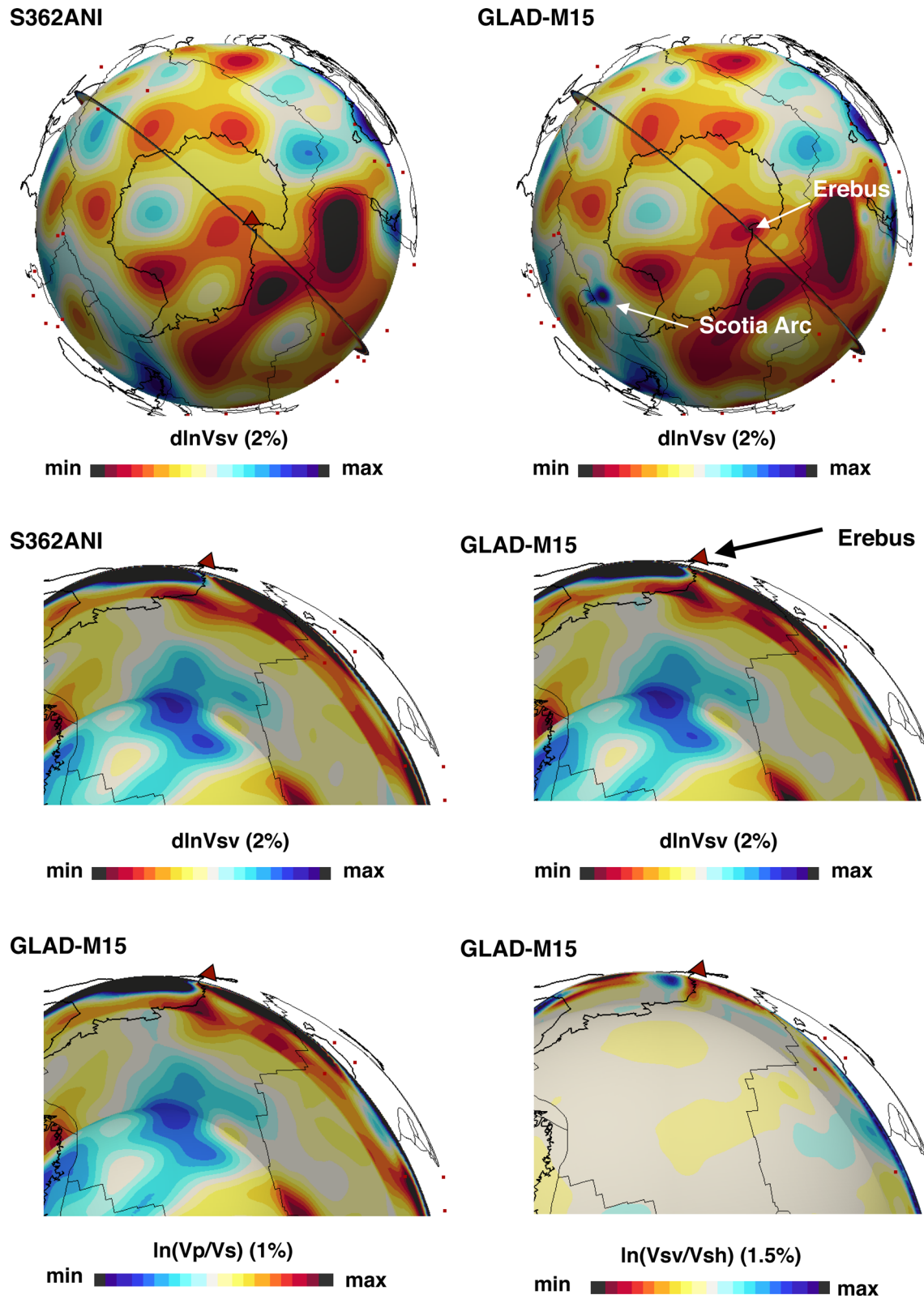


Figure 14. Map views at 450 km depth (top row) and vertical cross-sections (middle row) of vertically polarized shear-wave-speed perturbations in the starting model S362ANI+Crust2.0 and GLAD-M15 under Antarctica. Also shown are Vp/Vs ratios (bottom row, left) and transverse isotropy (bottom row, right). Map views in the middle and third row (left) denote the CMB, and the map view in the bottom right panel denotes the 660 km discontinuity, below which transverse isotropy vanishes. Each model is plotted relative to its own radial mean.

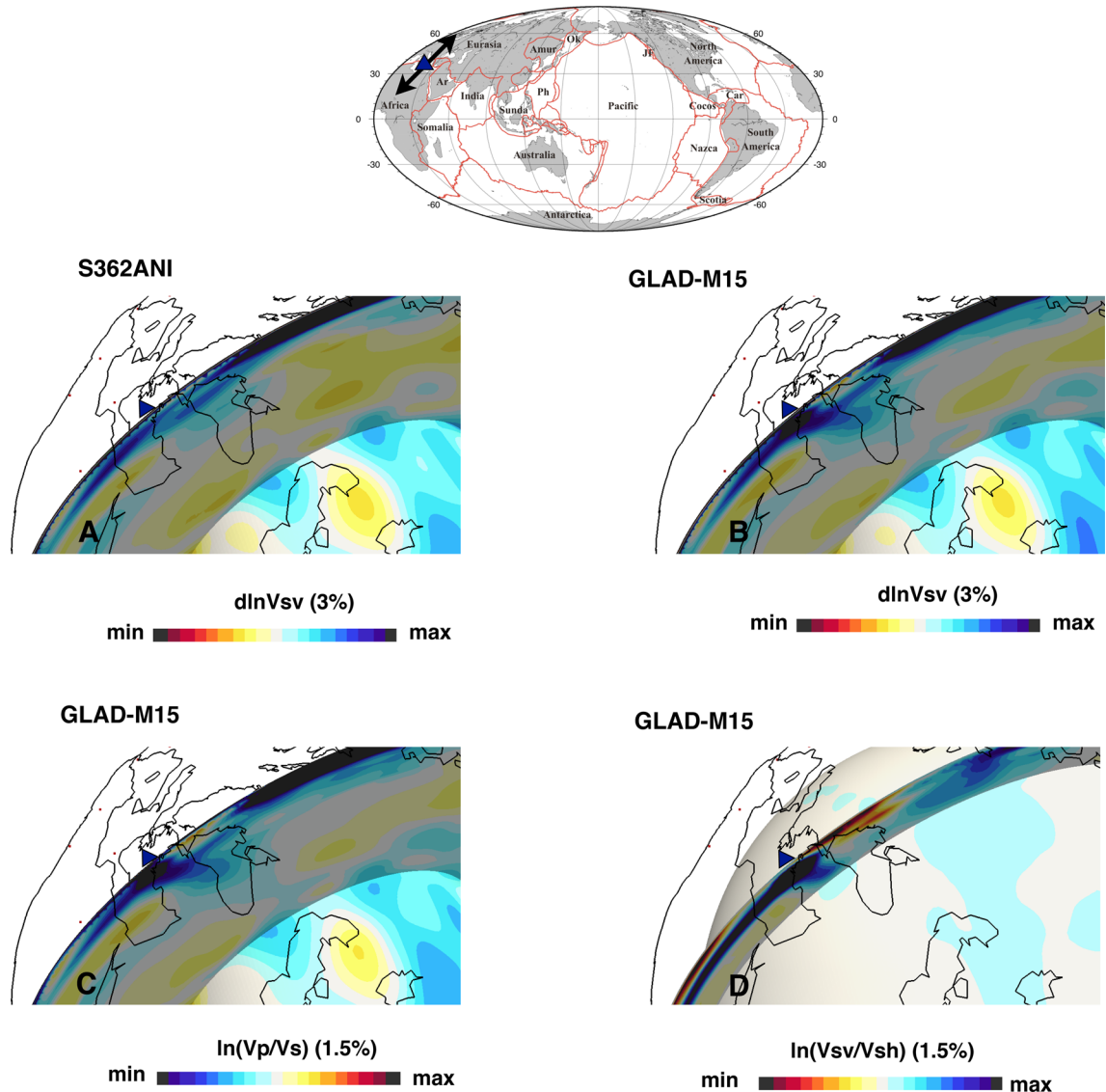


Figure 15. Cross-sections along the Hellenic Arc (top map) of vertically polarized shear-wave-speed perturbations in starting model S362ANI+Crust2.0 (middle row, left) and GLAD-M15 (middle row, right). Also shown are V_p/V_s ratios (bottom row, left) and transverse isotropy (bottom row, right). Map views in the middle and third row (left) denote the CMB, and the map view in the bottom right panel denotes the 660 km discontinuity, below which transverse isotropy vanishes. Each model is plotted relative to its own radial mean.

computed the difference between the gradients of the perturbed and unperturbed 14th-iteration models, thereby giving the action of the Hessian on the model parameters according to eqn. (10).

In Figs 18 and 19 we show the results for vertically polarized shear-wave-speed perturbations centred on Yellowstone and Erebus, respectively. The Gaussians are reasonably well retrieved without much bias or smearing in the upper mantle, which supports the resolution of the observed features. Furthermore, trade off with other model parameters mainly occurs as random noise near the surface and does not generate a significant anomaly at the location of perturbation.

5.6 Independent earthquake database

Following an approach used by Tape *et al.* (2009, 2010) and Chen *et al.* (2015), we further investigated the quality of our model with an independent database of 40 randomly selected $6.5 \leq M_w \leq 7.0$ earthquakes, shown in Fig. 20. We chose slightly larger events because these generate more measurements for analysis. An earthquake not

used in the tomographic inversion may be used to independently assess the misfit reduction from M00 to M15. In Fig. 21, we show multitaper (for dispersive waveforms) and cross-correlation (for non-dispersive waveforms) traveltime anomaly histograms for the final four measurement categories on all three components for starting model S362ANI+Crust2.0 (M00) and final model GLAD-M15 (M15). Like the histograms for the data used in the actual inversion (shown in Fig. 7), these histograms show a clear reduction in the traveltimes anomalies in M15 compared to M00 in the form of more sharply centred distributions in all 12 categories. This result provides validation for our global model and suggests that future earthquakes will see similar misfit reductions.

5.7 Comparisons with S40RTS

It is well known that global models differ significantly from each other at smaller scales. Detailed model comparisons may be found in numerous studies (e.g. Schaeffer & Lebedev 2013; Chang *et al.* 2014; French & Romanowicz 2015). Here, we present a

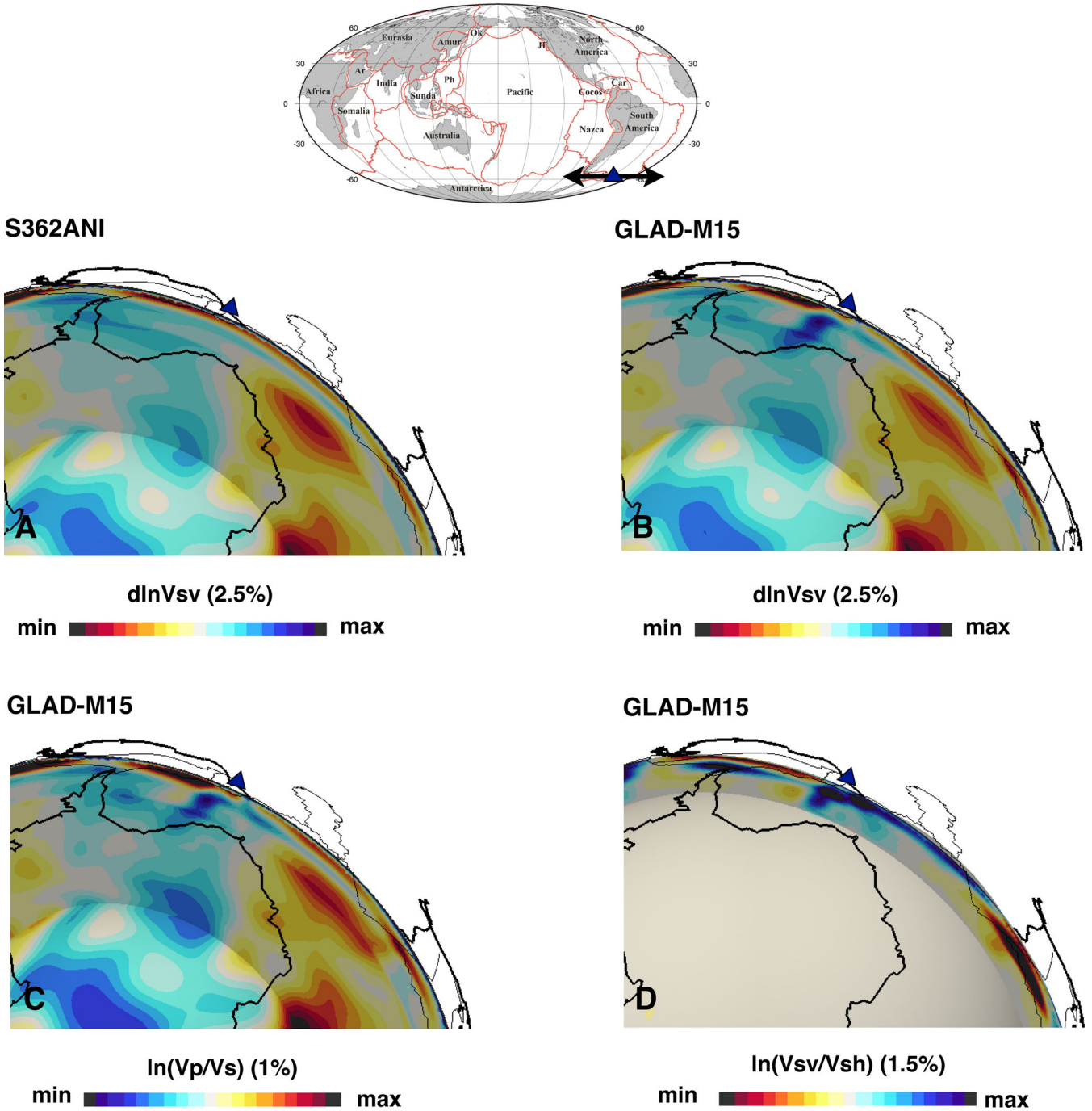


Figure 16. Same as Fig. 15, but for the Scotia Arc.

comparison with S40RTS (Ritsema *et al.* 2011), a recent degree-40 global model. In Figs 22 and 23, we show map views at various depths of our model together with starting model S362ANI (Kustowski *et al.* 2008) and S40RTS (Ritsema *et al.* 2011). We observe that our 15th-iteration model generally takes the common ground between S362ANI and S40RTS.

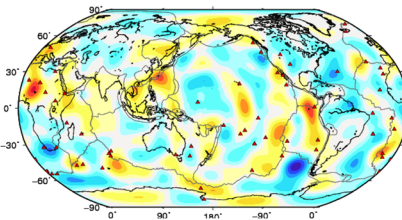
6 DISCUSSION

GLAD-M15 is the first global model based on fully 3-D forward and adjoint simulations of seismic wave propagation since

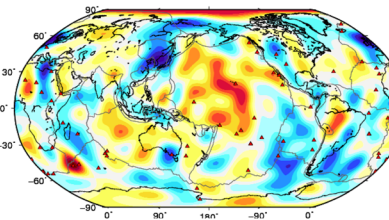
the inception of ‘FW’ by Tarantola (1984b). It naturally unifies the crust and mantle by inverting them jointly, using anything and everything in three-component seismograms that passes automated misfit and data-quality selection criteria. Many global models use bigger data sets in terms of the number of earthquakes (e.g. Schaeffer & Lebedev 2013), or merge various complementary secondary data types, such as phase and group wave speeds, traveltimes, and splitting functions, sometimes even including isolated waveforms (e.g. Ritsema *et al.* 2011; Chang *et al.* 2014). Our study demonstrates what is feasible with a limited data set of 253 earthquakes and just 15 tomographic iterations. Imagine what more can be done with the thousands of suitable

S362ANI

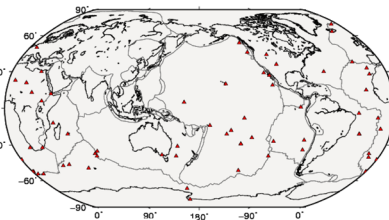
100 km (4%)



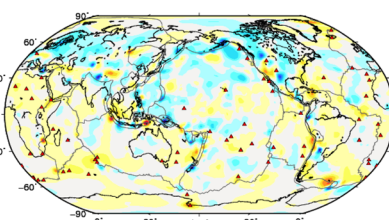
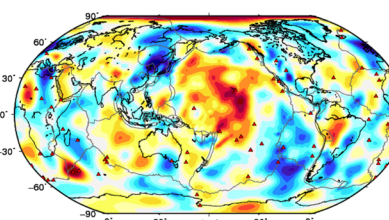
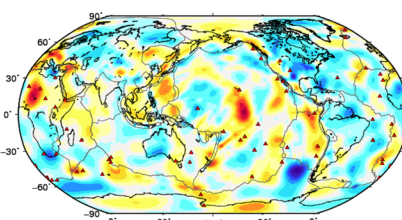
200 km (4%)



400 km (2%)

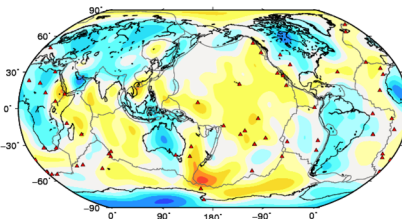


GLAD-M15

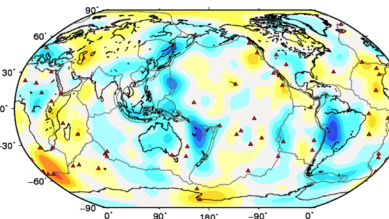
 $\ln(Vsv/Vsh)$ (%)

min — max

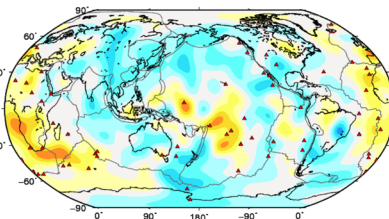
250 km (3%)



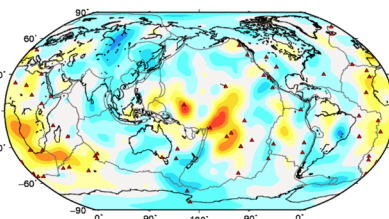
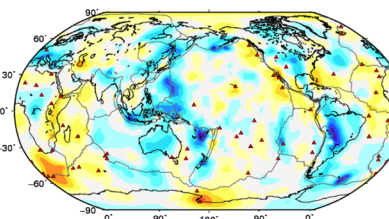
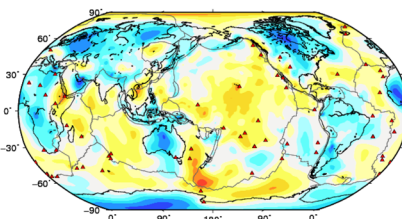
750 km (1.5%)



2400 km (1.5%)



S362ANI

 $\ln(Vp/Vs)$ (%)

min — max

Figure 17. Map views of transverse isotropy and Vp/Vs ratios at various depths in GLAD-M15 and starting mantle model S362ANI. Each model is shown with respect to its own mean.

earthquakes that have already been recorded by worldwide seismographic networks!

Granted, our approach is currently computationally expensive. However, we are at a stage where such expenses are justified,

even necessary. The significance of using full-attenuation in adjoint kernel simulations serves as a case in point: approximate kernels based on physical-dispersion only are inadequate for full-orbit surface waves. If the goal is to assimilate anything and everything,

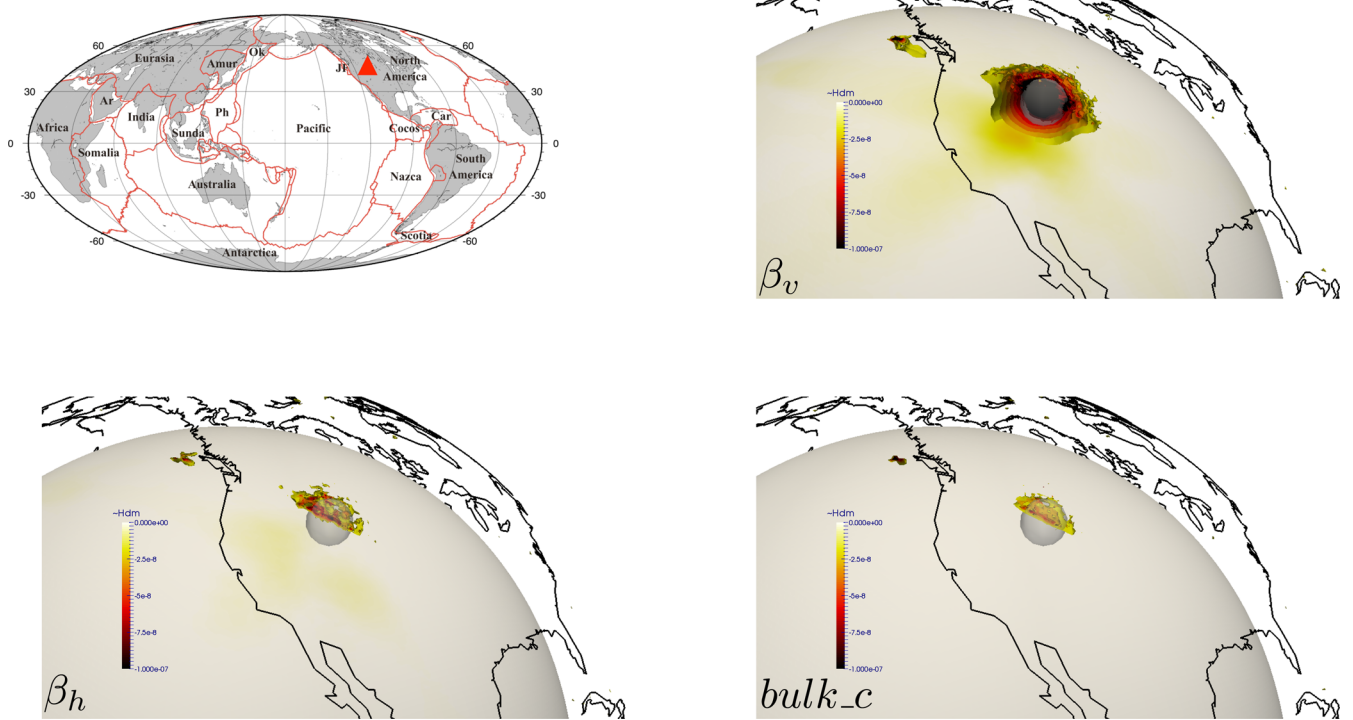


Figure 18. 3-D contour plot of a point-spread function to assess resolution at Yellowstone which is cut through to view the inside of the anomaly. The 14th iteration β_v model was perturbed by a 2 per cent spherical Gaussian located at 125 km depth with a radius of 250 km. Grey spheres denote the size of the spherical Gaussian, and a vertical section is taken on the contour plot to show the values on the inside. β_h and c plots in the bottom row show trade-offs with these model parameters. Map views denote 660 km discontinuity.

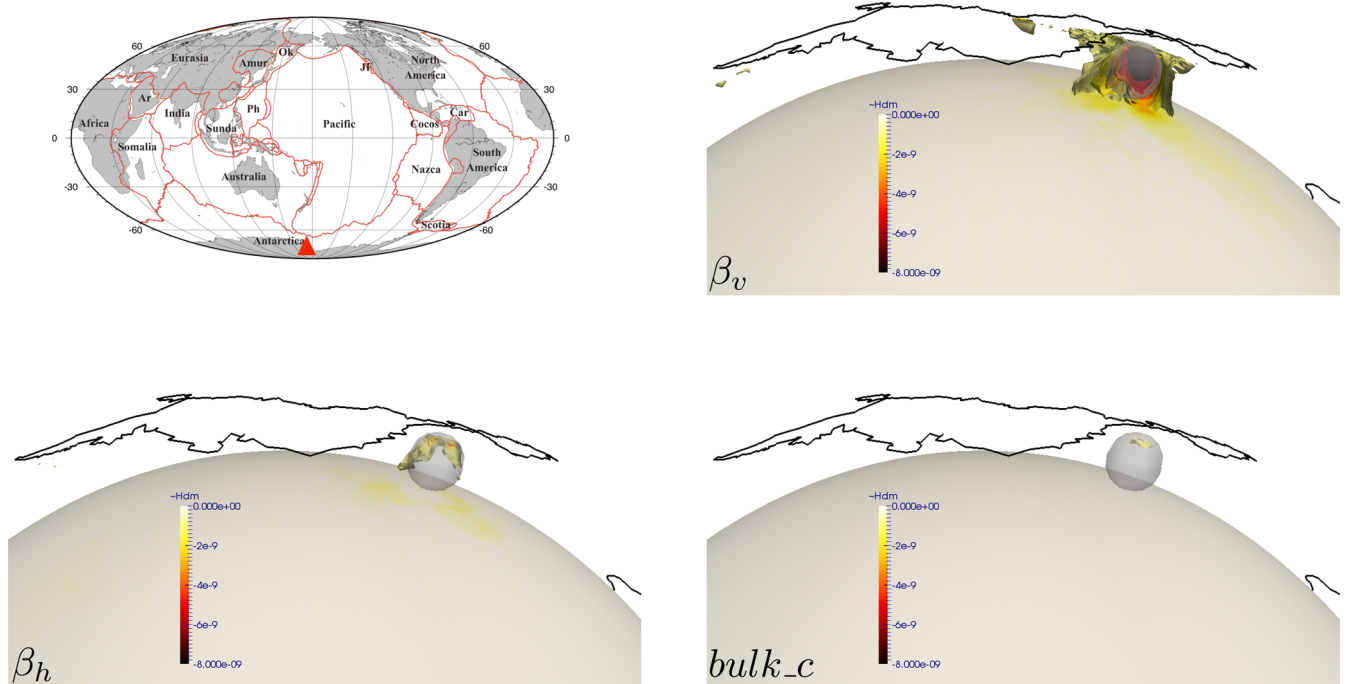


Figure 19. Same as Fig. 18, but for Erebus. The 14th iteration β_v model was perturbed by a 2 per cent spherical Gaussian located at 300 km depth with a radius of 300 km.

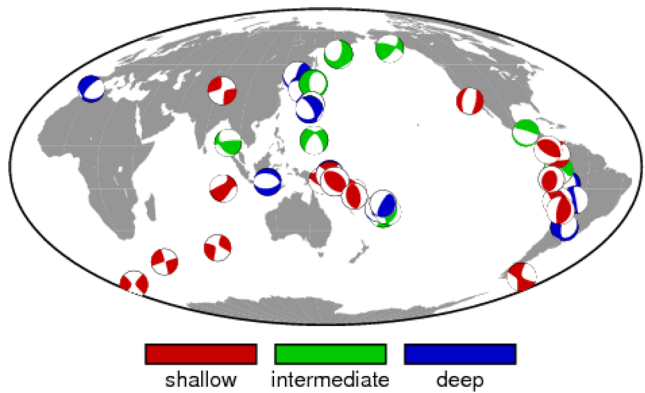


Figure 20. Collection of 40 independent global earthquakes ($6.5 \leq M_w \leq 7.0$) used to assess traveltime misfit in model GLAD-M15. These events were not used in the actual structural inversion.

synthetic seismograms must be calculated as accurately as possible to avoid errors in the forward theory from contaminating the model. And the advantage of adjoint-state methods is that they end up solving the fully 3-D nonlinear inverse problem, albeit iteratively and therefore not cheaply.

The impact of the starting model on FWI is well recognized. Since most global models are in agreement at long wavelengths (e.g. Ritzwoller & Lavelle 1995; Becker & Boschi 2002), we chose to start with such a model rather than a spherically symmetric model. Broadly speaking, our iterations only modify the starting model

where such modifications are warranted by the data, as expressed in the Fréchet derivatives. It is for this reason that we see much more detailed structural variations underneath North America and Europe in GLAD-M15, and the resolution of Erebus clearly benefited from temporary array deployments in Antarctica.

Despite the power of our approach, it remains a challenge to fit every wiggle in 180 min broad-band teleseismic seismograms both in phase and amplitude. More ocean-bottom seismometers or recently proposed floating acoustic sensors (e.g. Simons *et al.* 2009; Sukhovich *et al.* 2015) would of course help in terms of global coverage. Moreover there is still scope for improving imbalanced coverage and reducing uncertainties based on new measurement strategies (e.g. Choi & Alkhalifah 2012; Yuan *et al.* 2016). But the most natural way forward is to use all available data from all earthquakes in the global CMT catalogue. That data is readily available, and we should be using it all. In theory, there is no impediment to assimilating all suitable data in global adjoint tomography. In practice, we need robust workflows and modern data formats to make this possible, in addition to substantial computational resources. Workflow management and stabilization is an active area of research in computational science in general and computational seismology in particular (Lefebvre *et al.* 2014; Krischer *et al.* 2015a).

We currently take advantage of GPU computing by having access to more than 18K graphics cards on the Oak Ridge Leadership Computing Facility (OLCF) Cray ‘Titan’, a machine with a peak performance of more than 20 petaflops. Exascale computers are expected to become available in the 2020–2022 time frame, and we

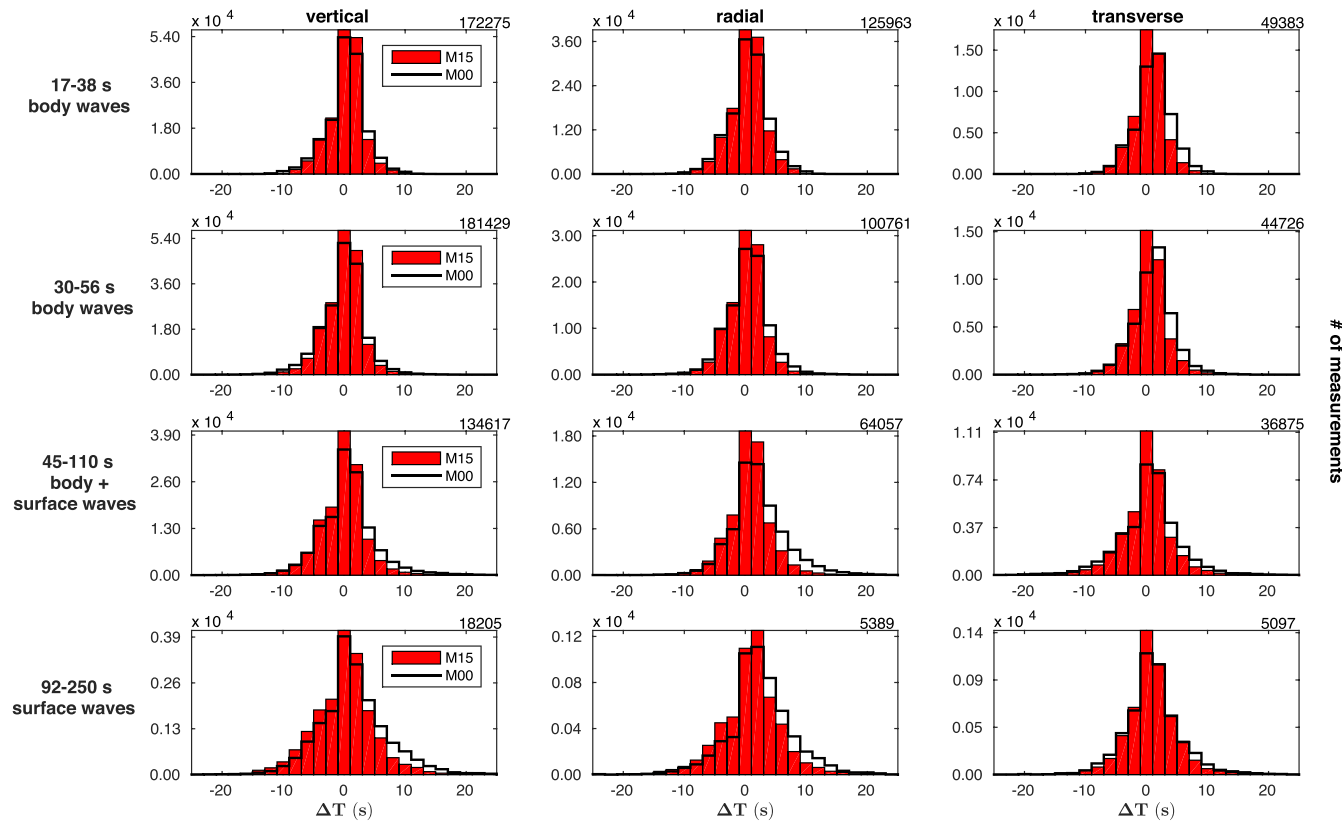


Figure 21. Same as Fig. 7, except for the set of 40 additional earthquakes shown in Fig. 20, which were not used in structural inversions. There are $\sim 938\,000$ measurements.

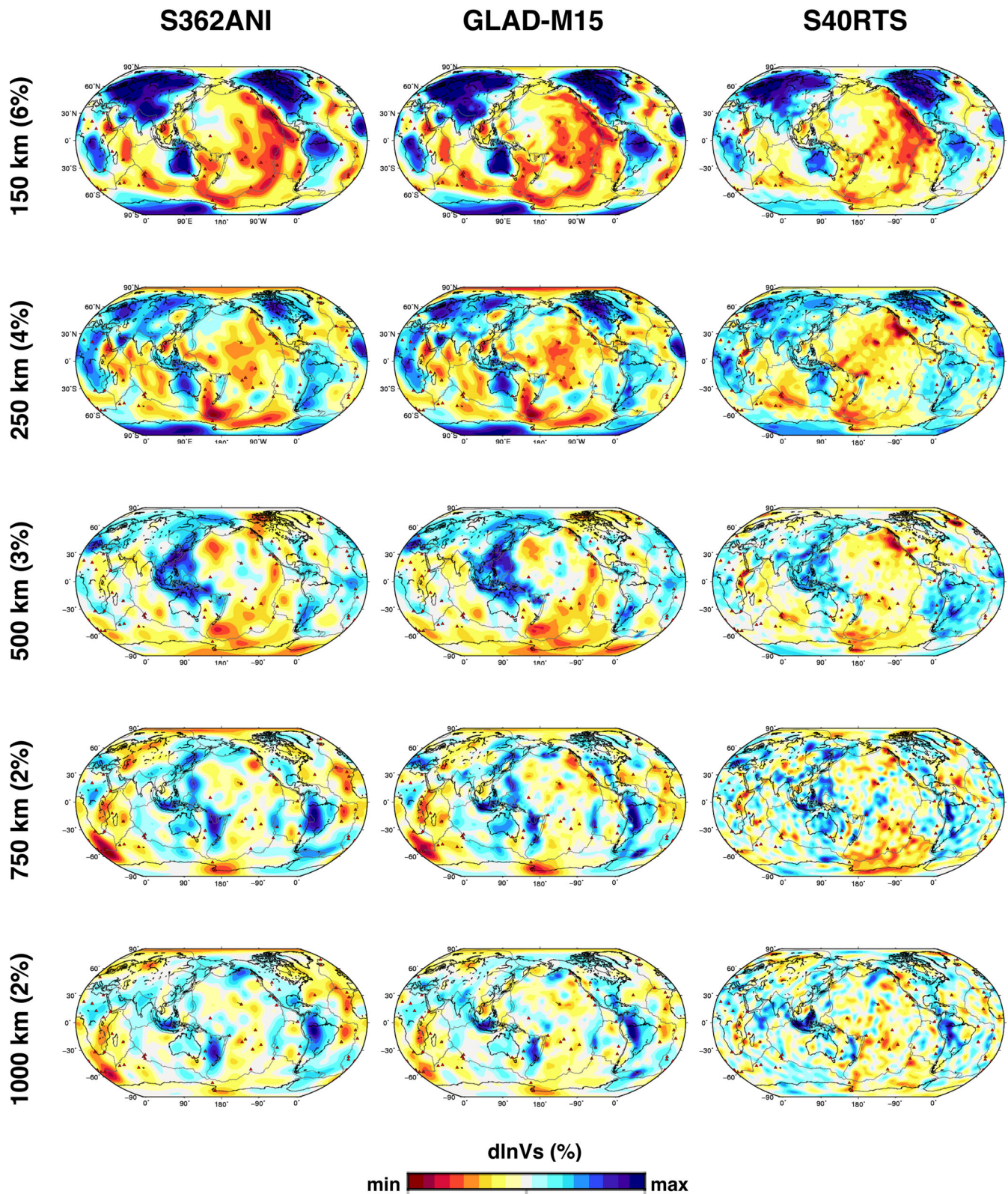


Figure 22. Comparison of horizontal isotropic shear-wave-speed cross-sections of GLAD-M15 with starting mantle model S362ANI and recent degree-40 mantle model S40RTS (Ritsema *et al.* 2011).

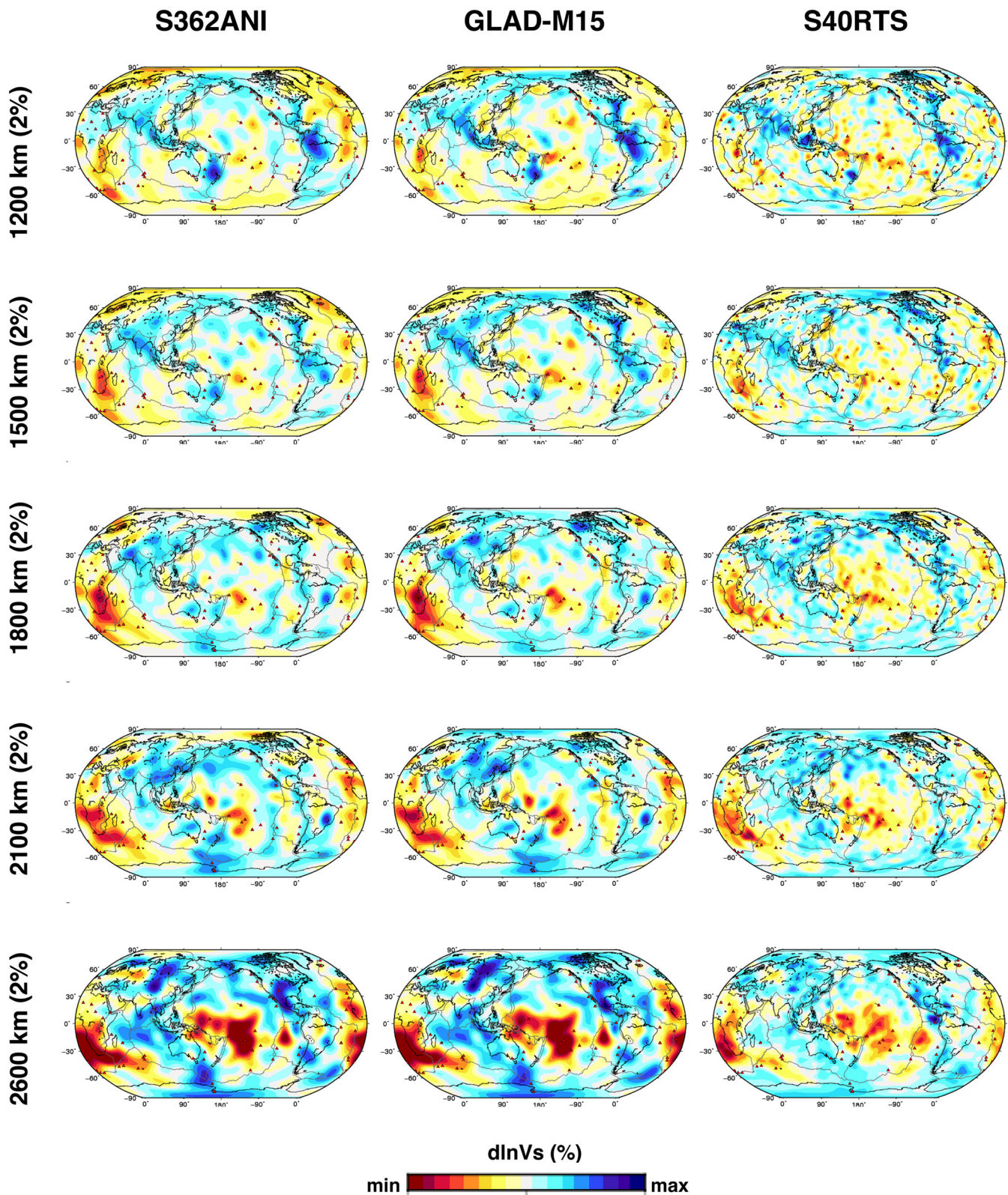


Figure 23. Same as Fig. 22, but for greater depths.

want to be ready to harness such systems when they do. Needless to say, this requires continual investments in code development and optimization. With this goal in mind, we are a partner in ORNL's Center for Accelerated Application Readiness (CAAR). CAAR has established eight partnerships to prepare computational science & engineering applications for use on the OLCF system to be named 'Summit', which will become available in 2018. The Summit system, an IBM with Power-9 CPUs and NVIDIA Volta GPU accelerators, will help determine what exascale hardware might look like in the early 2020s. Summit will enable us to reduce the shortest period in our global simulations from 17 to 9 s, and exascale systems will reduce this further to just a few seconds.

Tomographic resolution depends in part on the chosen model parametrization. To make the problem tractable, we currently keep the 1-D Q model constant in numerical simulations and assume that the Earth is elastic with transverse isotropy confined to the upper mantle, and use (frequency-dependent) phase information only. The PSF tests confirm that such inversions are feasible with the current data set. Building on our experiences in Europe (Zhu *et al.* 2013; Zhu & Tromp 2013), we plan to invert for global azimuthal anisotropy and attenuation in the future. In the latter case, we will investigate the inclusion of frequency-dependent amplitude measurements.

7 CONCLUSIONS AND FUTURE WORK

We determined the first global tomographic model based on fully 3-D forward and adjoint simulations of anelastic seismic wave propagation. We assimilated 3.8 million measurements in three-component data from 253 earthquakes with a shortest period of 17 s, using 180 min seismograms containing full-orbit surface waves. Our 'first generation' model is the result of 15 conjugate-gradient iterations performed on the Cray XK7 'Titan', a supercomputer located at Oak Ridge National Laboratory (USA). We simultaneously inverted for crust and mantle structure, thereby avoiding 'crustal corrections'; thus ours is the first global model which naturally unifies the crust and mantle. The model is transversely isotropic in the upper mantle, and contains numerous distinct signatures of plumes, hotspots, and slabs. Such anomalies are seen in lateral variations in shear wave speed, but also in the Vp/Vs ratio and in transverse isotropy. Our multiscale smoothing strategy helps bring out smaller-scale features where coverage is good, for example, underneath USArray. Point-spread function tests show that a number of interesting features are well resolved in our models, with limited parameter trade off. Finally, we used a data set of 40 additional earthquakes not used in the construction of our global model to demonstrate that it provides a clear improvement in traveltimes fit compared to the starting model.

Looking forward, our goal is to assimilate data from thousands of earthquakes that have already been recorded by global and regional networks. This requires further optimizing and stabilizing the adjoint tomography workflow by taking advantage of workflow management tools, such as Pegasus (pegasus.isi.edu).

ACKNOWLEDGEMENTS

EB dedicates this manuscript to her parents, Zahire & Hilmi Bozdağ. This research used resources of the Oak Ridge Leadership Computing Facility, which is a DOE Office of Science User Facility supported under contract DE-AC05-00OR22725. Additional computational resources were provided by the Princeton Institute for Computational Science & Engineering (PICSciE). We acknowledge

IRIS (iris.edu) and ORFEUS (orfeus-eu.org) for providing the data used in this study. We gratefully acknowledge editor Gabi Laske, Carl Tape and an anonymous reviewer for constructive feedback which improved the manuscript. We thank Heiner Igel, Suzan van der Lee, Guust Nolet, Jeroen Ritsema, Frederik J. Simons and Jeannot Trampert for their support and fruitful discussions. We also thank Wenjie Lei and Youyi Ruan for providing 40 reinverted CMT solutions for tests with an independent set of earthquakes, and Yanhua Yuan, Ryan Modrak, Vadim Monteiller, Lion Krischer and James Smith for various discussions on FWI. The open source spectral-element software package SPECFEM3D_GLOBE and the seismic measurement software package FLEXWIN used for this article are freely available via the Computational Infrastructure for Geodynamics (CIG; geodynamics.org). This research was supported by NSF grant 1112906. EB was partly supported by her UNS–CNRS Chaire d'Excellence grant.

REFERENCES

- Afanasiev, M., Peter, D., Sager, K., Simut, S., Ermert, L., Krischer, L. & Fichtner, A., 2015. Foundations for a multiscale collaborative Earth model, *Geophys. Res. Lett.*, **204**, 39–58.
- Akçelik, V., Biros, G. & Ghattas, O., 2002. Parallel multiscale Gauss–Newton–Krylov methods for inverse wave propagation, in *Proc. ACM/IEEE Supercomputing SC'2002 Conference*, IEEE, Los Alamitos, CA, published at www.sc-conference.org/sc2002.
- Akçelik, V. *et al.*, 2003. High resolution forward and inverse earthquake modeling on terascale computers, in *Proc. ACM/IEEE Supercomputing SC'2003 Conference*, ACM, New York, NY, published at www.sc-conference.org/sc2003.
- Aki, K., Christoffersson, A. & Husebye, E.S., 1977. Determination of the three-dimensional seismic structure of the lithosphere, *J. geophys. Res.*, **82**, 277–296.
- Amante, C. & Eakins, B., 2009.ETOPO1 1 Arc-minute global relief model: Procedures, data sources and analysis, Tech. Rep., NOAA.
- Babuška, V. & Cara, M., 1991. *Seismic Anisotropy in the Earth*, Kluwer Academic Press.
- Backus, G.E., 1962. Long-wave elastic anisotropy produced by horizontal layering, *J. geophys. Res.*, **67**, 4427–4440.
- Bamberger, A., Chavent, G. & Lailly, P., 1977. Une application de la théorie du contrôle à un problème inverse sismique, *Ann. Geophys.*, **33**, 183–200.
- Bassin, C., Laske, G. & Masters, G., 2000. The current limits of resolution for surface wave tomography in North America, *EOS, Trans. Am. geophys. Un.*, **81**, F897.
- Becker, T.W. & Boschi, L., 2002. A comparison of tomographic and geodynamic mantle models, *Geochem. Geophys. Geosyst.*, **3**(1), 1003, doi:10.1029/2001GC000168.
- Bijwaard, H. & Spakman, W., 2000. Nonlinear global P-wave tomography by iterated linearized inversion, *Geophys. J. Int.*, **141**, 71–82.
- Bird, P., 2003. An updated digital model of plate boundaries, *Geochem. Geophy. Geosyst.*, **4**, 1–52.
- Boschi, L. & Dziewoński, A.M., 2000. Whole Earth tomography from delay times of P, P_cP and PKP phases: lateral heterogeneities in the outer core and radial anisotropy in the mantle?, *J. geophys. Res.*, **105**(B6), 13 675–13 696.
- Boschi, L. & Ekström, G., 2002. New images of the Earth's upper mantle from measurements of surface-wave phase velocity anomalies, *J. geophys. Res.*, **107**(B4), 2059, doi:10.1029/2000JB000059.
- Bozdağ, E. & Trampert, J., 2008. On crustal corrections in surface wave tomography, *Geophys. J. Int.*, **172**, 1066–1082.
- Bozdağ, E., Trampert, J. & Tromp, J., 2011. Misfit functions for full waveform inversions based on instantaneous phase and envelope measurements, *Geophys. J. Int.*, **185**, 845–870.
- Brossier, R., Operto, S. & Virieux, J., 2009. Seismic imaging of complex onshore structures by 2D elastic frequency-domain full-waveform inversion, *Geophysics*, **74** (6), WCC105–WCC118.

- Capdeville, Y. & Marigo, J.-J., 2007. Second order homogenization of the elastic wave equation for non-periodic layered media, *Geophys. J. Int.*, **170**, 823–838.
- Capdeville, Y., Chaljub, E., Villette, J.P. & Montagner, J.P., 2003. Coupling the spectral element method with a modal solution for elastic wave propagation in global earth models, *Geophys. J. Int.*, **152**, 34–67.
- Chaljub, E. & Valette, B., 2004. Spectral element modelling of three-dimensional wave propagation in a self-gravitating Earth with an arbitrarily stratified outer core, *Geophys. J. Int.*, **158**, 131–141.
- Chaljub, E., Capdeville, Y. & Villette, J.P., 2003. Solving elastodynamics in a fluid-solid heterogeneous sphere: a parallel spectral-element approximation on non-conforming grids, *J. Comput. Phys.*, **187**(2), 457–491.
- Chang, S.J., Ferreira, A.M.G., Ritsema, J., van Heijst, H.J. & Woodhouse, J.H., 2014. Global radially anisotropic mantle structure from multiple datasets: A review, current challenges, and outlook, *Tectonophysics*, **617**, 1–19.
- Chang, S.-J., Ferreira, A.M.G. & Faccenda, M., 2016. Upper- and mid-mantle interaction between the Samoan plume and the Tonga-Kermadec slabs, *Nat. Comm.*, **7**, 10799, doi:10.1038/ncomms10799.
- Chavent, G., 1974. Identification of parameter distributed systems, in *Identification of Function Parameters in Partial Differential Equations*, pp. 31–48, eds Goodson, R.E. & Polis, M., American Society of Mechanical Engineers.
- Chen, M., Niu, F., Liu, Q., Tromp, J. & Zheng, X., 2015. Multi-parameter adjoint tomography of the crust and upper mantle beneath East Asia: Part I: Model construction and comparisons, *J. geophys. Res.*, **120**(3), 1762–1786.
- Choi, Y. & Alkhalifah, T., 2012. Source-independent time-domain waveform inversion using convolved wavefields: application to the encoded multi-source waveform inversion, *Geophysics*, **76**, 125–134.
- Cowling, T.G., 1941. The non-radial oscillations of polytropic stars, *Mon. Not. R. Astron. Soc.*, **101**, 369–373.
- Dahlen, F., Nolet, G. & Hung, S., 2000. Fréchet kernels for finite-frequency traveltimes—I. Theory, *Geophys. J. Int.*, **141**, 157–174.
- Dahlen, F.A. & Baig, A.M., 2002. Fréchet kernels for body-wave amplitudes, *Geophys. J. Int.*, **150**, 440–466.
- Deelman, E. et al., 2015. Pegasus, a workflow management system for science automation, *Future Gener. Comput. Syst.*, **46**, 17–35.
- Dziewoński, A.M., 1984. Mapping the lower mantle: determination of lateral heterogeneity in P velocity up to degree and order 6, *J. geophys. Res.*, **89**, 5929–5952.
- Dziewoński, A.M. & Anderson, D.L., 1981. Preliminary reference Earth model, *Phys. Earth planet. Inter.*, **25**, 297–356.
- Dziewoński, A.M., Hager, B.H. & O'Connell, R.J., 1977. Large-scale heterogeneities in the lower mantle, *J. geophys. Res.*, **82**, 239–255.
- Ekström, G., 2011. A global model of Love and Rayleigh surface wave dispersion and anisotropy, 25–250 s, *Geophys. J. Int.*, **187**, 1668–1686.
- Ekström, G., Tromp, J. & Larson, E. W.F., 1997. Measurements and global models of surface wave propagation, *J. geophys. Res.*, **102**, 8137–8157.
- Faccenna, C., Becker, T.W., Lallemand, S., Lagabrielle, Y., Funiciello, F. & Piromallo, C., 2010. Subduction-triggered magmatic pulses: a new class of plumes?, *Earth planet. Sci. Lett.*, **299**, 54–68.
- Ferreira, A.M.G., Woodhouse, J.H., Visser, K. & Trampert, J., 2010. On the robustness of global radially anisotropic surface wave tomography, *J. geophys. Res.*, **115**(B4), 1–16.
- Fichtner, A. & Trampert, J., 2011. Resolution analysis in full waveform inversion, *Geophys. J. Int.*, **187**, 1604–1624.
- Fichtner, A. & van Leeuwen, T., 2015. Resolution analysis by random probing, *J. geophys. Res.*, **120**, 5549–5573.
- Fichtner, A., Bunge, H.-P. & Igel, H., 2006a. The adjoint method in seismology—I. Theory, *Phys. Earth planet. Inter.*, **157**, 86–104.
- Fichtner, A., Bunge, H.-P. & Igel, H., 2006b. The adjoint method in seismology—II. Applications: traveltimes and sensitivity functionals, *Phys. Earth planet. Inter.*, **157**, 105–123.
- Fichtner, A., Kennett, B.L.N. & Bunge, H.-P., 2008. Theoretical background for continental and global scale full-waveform inversion in the time-frequency domain, *Geophys. J. Int.*, **175**, 665–685.
- Fichtner, A., Kennett, B.L.N., Igel, H. & Bunge, H.-P., 2009. Full seismic waveform tomography for upper-mantle structure in the Australasian region using adjoint methods, *Geophys. J. Int.*, **179**, 1703–1725.
- Fichtner, A., Trampert, J., Cupillard, P., Saygin, E., Taymaz, T., Capdeville, Y. & Villaseñor, A., 2013. Multiscale full waveform inversion, *Geophys. J. Int.*, **194**, 534–556.
- Fletcher, R. & Reeves, C.M., 1964. Function minimization by conjugate gradients, *Comput. J.*, **7**, 149–154.
- Fouch, M.J., 2012. The Yellowstone Hotspot: Plume or Not?, *Geophys. J. Int.*, **40**(5), 479–480.
- French, S.W. & Romanowicz, B., 2015. Broad plumes rooted at the base of the Earth's mantle beneath major hotspots, *Nature*, **525**, 95–99.
- French, S.W. & Romanowicz, B.A., 2014. Whole-mantle radially anisotropic shear velocity structure from spectral-element waveform tomography, *Geophys. J. Int.*, **199**(3), 1303–1327.
- French, S.W., Lekic, V. & Romanowicz, B., 2013. Waveform tomography reveals channeled flow at the base of the oceanic asthenosphere, *Science*, **342**, 227–230.
- Gauthier, O., Virieux, J. & Tarantola, A., 1986. Two-dimensional nonlinear inversion of seismic waveforms: numerical results, *Geophysics*, **51**, 1387–1403.
- Gee, L. & Jordan, T.H., 1992. Generalized seismological data functionals, *Geophys. J. Int.*, **111**, 363–390.
- Gu, Y.J., Dziewoński, A.M., Su, W. & Ekstrom, G., 2001. Models of the mantle shear velocity and discontinuities in the pattern of lateral heterogeneity, *J. geophys. Res.*, **106**, 11 169–11 199.
- He, X. & Tromp, J., 1996. Normal mode constraints on the structure of the earth, *J. geophys. Res.*, **101**, 20 053–20 082.
- Helffrich, G., Wookey, J. & Bastow, I., 2013. *The Seismic Analysis Code: A Primer and User's Guide*, 1st edn, Cambridge Univ. Press.
- Hjorleifsdóttir, V. & Ekström, G., 2010. Effects of three-dimensional Earth structure on CMT earthquake parameters, *Phys. Earth planet. Inter.*, **179**, 178–190.
- Houser, C., Masters, G., Shearer, P.M. & Laske, G., 2008. Shear and compressional velocity models of the mantle from cluster analysis of long period waveforms, *Geophys. J. Int.*, **174**, 195–212.
- Kennett, B., Widjiantoro, S. & van der Hilst, R., 1998. Joint seismic tomography for bulk sound and shear wave speed in the Earth's mantle, *J. geophys. Res.*, **103**, 12 469–12 493.
- Kim, Y., Liu, Q. & Tromp, J., 2011. Adjoint centroid-moment tensor inversions, *Geophys. J. Int.*, **186**, 264–278.
- Koelemeijer, P., Ritsema, J., Deus, A. & van Heijst, H.J., 2016. SP12RTS: a degree-12 model of shear- and compressional-wave velocity for Earth's mantle, *Geophys. J. Int.*, **204**(2), 1024–1039.
- Komatitsch, D., 2011. Fluid-solid coupling on a cluster of GPU graphics cards for seismic wave propagation, *C. R. Acad. Sci. Ser. IIb Mec.*, **339**(2), 125–135.
- Komatitsch, D. & Tromp, J., 2002a. Spectral-element simulations of global seismic wave propagation – I. Validation, *Geophys. J. Int.*, **149**(2), 390–412.
- Komatitsch, D. & Tromp, J., 2002b. Spectral-element simulations of global seismic wave propagation – II. 3-D models, oceans, rotation, and self-gravitation, *Geophys. J. Int.*, **150**(1), 303–318.
- Komatitsch, D., Erlebacher, G., Göddeke, D. & Michéa, D., 2010. High-order finite-element seismic wave propagation modeling with MPI on a large GPU cluster, *J. Comput. Phys.*, **229**(20), 7692–7714.
- Komatitsch, D., Xie, Z., Bozdağ, E., de Andrade, E.S., Peter, D., Liu, Q. & Tromp, J., 2016. Anelastic sensitivity kernels with parsimonious storage for full waveform inversion and adjoint tomography, *Geophys. J. Int.*, **206**, 1467–1478.
- Krischer, L., Fichtner, A., Zukauskaite, S. & Igel, H., 2015a. Large-Scale Seismic Inversion Framework, *Seismol. Res. Lett.*, **86**(4), doi:10.1785/0220140248.
- Krischer, L., Megies, T., Barsch, R., Beyreuther, M., Lecocq, T., Caudron, C. & Wassermann, J., 2015b. ObsPy: a bridge for seismology into the scientific Python ecosystem, *Comput. Sci. Discovery*, **8**(1), 014003, doi:10.1088/1749-4699/8/1/014003.

- Krischer, L. *et al.*, 2016. An Adaptable Seismic Data Format, *Geophys. J. Int.*, **207**(2), 1003–1011.
- Kristekova, M., Kristek, J., Moczo, P. & Day, S., 2006. Misfit criteria for quantitative comparison of seismograms, *Bull. seism. Soc. Am.*, **96**(5), 1836–1850.
- Kustowski, B., Ekström, G. & Dziewoński, A.M., 2008. Anisotropic shear-wave velocity structure of the Earth's mantle: a global model, *J. geophys. Res.*, **113**, B06306, doi:10.1029/2007JB005169.
- Lailly, P., 1983. The seismic inverse problem as a sequence of before stack migration, in *Conference on Inverse Scattering: Theory and Application*, pp. 206–220, ed. Bednar, J., SIAM.
- Laske, G., Masters, G., Ma, Z. & Pasyanos, M., 2013. Update on CRUST1.0—A 1-degree Global Model of Earth's Crust, *Geophys. Res. Abstr.*, **15**, Abstract EGU2013–2658.
- Lebedev, S. & van der Hilst, R., 2008. Global upper-mantle tomography with the automated multimode inversion of surface and S-wave forms, *Geophys. J. Int.*, **173**, 505–518.
- Lebedev, S., Nolet, G., Meier, T. & van der Hilst, R., 2005. Automated multimode inversion of surface and S waveforms, *Geophys. J. Int.*, **162**, 951–964.
- Lee, E.-J. & Chen, P., 2013. Automating seismic waveform analysis for full 3-D waveform inversions, *Geophys. J. Int.*, **194**, 572–589.
- Lee, E.-J., Chen, P., Jordan, T.H., Maeckling, P.B., Denolle, M.A.M. & Beroza, G.C., 2014. Full-3-D tomography for crustal structure in Southern California based on the scattering-integral and the adjoint-wavefield methods, *J. geophys. Res.*, **119**, 6421–6451.
- Lefebvre, M. *et al.*, 2014. A data centric view of large-scale seismic imaging workflows, in *4th SC Workshop on Petascale Data Analytics*, July 20–25, Barcelona, Spain, Invited Paper.
- Lekić, V. & Romanowicz, B., 2011. Inferring upper-mantle structure by full waveform tomography with the spectral element method, *Geophys. J. Int.*, **185**(2), 799–831.
- Lekić, V., Panning, M. & Romanowicz, B., 2010. A simple method for improving crustal corrections in waveform tomography, *Geophys. J. Int.*, **182**, 265–278.
- Li, C., van der Hilst, R.D., Engdahl, E.R. & Burdick, S., 2008. A new global model for P wave speed variations in Earth's mantle, *Geochem. Geophys. Geosys.*, **9**(5), Q05018, doi:10.1029/2007GC001806.
- Li, X.-D. & Romanowicz, B., 1996. Global mantle shear velocity model developed using nonlinear asymptotic coupling theory, *J. geophys. Res.*, **101**(B10), 22,245–22,272.
- Liu, Q. & Tromp, J., 2006. Finite-frequency kernels based on adjoint methods, *Bull. seism. Soc. Am.*, **96**(6), 2383–2397.
- Liu, Q., Polet, J., Komatitsch, D. & Tromp, J., 2004. Spectral-element moment tensor inversions for earthquakes in Southern California, *Bull. seism. Soc. Am.*, **94**(5), 1748–1761.
- Liu, Q. *et al.*, 2014. Hello ADIOS: the challenges and lessons of developing leadership class I/O frameworks, *Concurrency Comput., Pract. Exp.*, **26**(7), 1453–1473.
- Loiselet, C., Braun, J., Husson, L., de Veslud, C.L.C., Thieulot, C., Yamato, P. & Gruijic, D., 2010. Subducting slabs: Jellyfishes in the Earth's mantle, *Geochem. Geophys. Geosyst.*, **11**(8), Q08016, doi:10.1029/2010GC003172.
- Love, A.E.H., 1927. *A Treatise on the Mathematical Theory of Elasticity*, 4th edn, Cambridge Univ. Press.
- Luo, Y. & Schuster, G.T., 1991. Wave-equation traveltimes inversion, *Geophysics*, **56**, 645–653.
- Luo, Y., Modrak, R. & Tromp, J., 2013. Strategies in Adjoint Tomography, *Handbook of Geomathematics*, 2nd edn, eds Freeden, W., Nahed, Z. & Sonar, T., Springer.
- Maggi, A., Tape, C., Chen, M., Chao, D. & Tromp, J., 2009. An automated time window selection algorithm for seismic tomography, *Geophys. J. Int.*, **178**, 257–281.
- Marquering, H., Dahlen, F. & Nolet, G., 1999. Three-dimensional sensitivity kernels for finite-frequency traveltimes: the banana-doughnut paradox, *Geophys. J. Int.*, **137**, 805–815.
- Mégnin, C. & Romanowicz, B., 2000. The three-dimensional shear velocity structure of the mantle from the inversion of body, surface and higher-mode waveforms, *Geophys. J. Int.*, **143**, 709–728.
- Merzky, A., Santcroos, M., Turilli, M. & Jha, S., 2016. Executing dynamic and heterogeneous workloads on super computers, under review, <http://arxiv.org/abs/1512.08194>.
- Modrak, R. & Tromp, J., 2016. Seismic waveform inversion best practices: regional, global, and exploration test cases, *Geophys. J. Int.*, **206**, 1864–1889.
- Montagner, J.-P. & Jobert, N., 1988. Vectorial tomography – II. Application to the Indian Ocean, *Geophys. Res. Lett.*, **94**, 309–344.
- Montagner, J.-P., 1998. Where can seismic anisotropy be detected in the Earth's mantle? In boundary layers ..., *Pure appl. Geophys.*, **151**, 223–256.
- Montagner, J.-P. & Anderson, D., 1989. Petrological constraints on seismic anisotropy, *Phys. Earth planet. Inter.*, **54**, 82–105.
- Monteiller, V., Chevrot, S., Komatitsch, D. & Wang, Y., 2015. Three-dimensional full waveform inversion of short-period teleseismic wavefields based upon the SEM-DSM hybrid method, *Geophys. J. Int.*, **202**(2), 811–827.
- Montelli, R., Nolet, G., Dahlen, F., Masters, G., Engdahl, E.R. & Hung, S.-H., 2004. Finite-frequency tomography reveals a variety of plumes in the mantle, *Science*, **303**, 338–343.
- Moulik, P. & Ekström, G., 2014. An anisotropic shear velocity model of the Earth's mantle using normal modes, body waves, surface waves and long-period waveforms, *Geophys. J. Int.*, **199** (3), 1713–1738.
- Moulik, P. & Ekström, G., 2016. The relationships between large-scale variations in shear velocity, density, and compressional velocity in the Earth's mantle, *J. geophys. Res.*, **121**, 2737–2771.
- Nocedal, J., 1980. Updating quasi-Newton matrices with limited storage, *Math. Comput.*, **35**, 773–782.
- Nolet, G., 1987. Waveform tomography, in *Seismic Tomography: With Applications in Global Seismology and Exploration Geophysics*, pp. 301–322, ed. Nolet, G., Reidel Publishing.
- Nolet, G., van Trier, J. & Huisman, R., 1986. A formalism for nonlinear inversion of seismic surface waves, *Geophys. Res. Lett.*, **13**, 26–29.
- Pageot, D., Operto, S., Vallée, M., Brossier, R. & Virieux, J., 2013. A parametric analysis of two-dimensional elastic full waveform inversion of teleseismic data for lithospheric imaging, *Geophys. J. Int.*, **193**(3), 1479–1505.
- Panning, M.P., Lekić, V. & Romanowicz, B., 2010. Importance of crustal corrections in the development of a new global model of radial anisotropy, *J. geophys. Res.*, **115**, B12325, doi:10.1029/2010JB007520.
- Peter, D. *et al.*, 2011. Forward and adjoint simulations of seismic wave propagation on fully unstructured hexahedral meshes, *Geophys. J. Int.*, **186**(2), 721–739.
- Pierce, K.L. & Morgan, L.A., 2009. Is the track of the Yellowstone hotspot driven by a deep mantle plume? Review of volcanism, faulting, and uplift in light of new data, *J. Volcanol. Geotherm. Res.*, **188**, 1–25.
- Plessix, R.E., 2009. Three-dimensional frequency-domain full-waveform inversion with an iterative solver, *Geophysics*, **74**(6), WCC53–WCC61.
- Pratt, R.G. & Shipp, R.M., 1999. Seismic waveform inversion in the frequency domain, Part 2: Fault delineation in sediments using crosshole data, *Geophysics*, **64**, 902–914.
- Prieux, V., Lambaré, G., Operto, S. & Virieux, J., 2013. Building starting models for full waveform inversion from wide-aperture data by stereotomography, *Geophys. Prospect.*, **61**, 109–137.
- Rickers, F., Fichtner, A. & Trampert, J., 2012. Imaging mantle plumes with instantaneous phase measurements of diffracted waves, *Geophys. J. Int.*, **190**, 650–664.
- Ritsema, J., van Heijst, H.J. & Woodhouse, J.H., 1999. Complex shear velocity structure imaged beneath Africa and Iceland, *Science*, **286**, 1925–1928.
- Ritsema, J., Rivera, L.A., Komatitsch, D., Tromp, J. & van Heijst, H.-J., 2002. Effects of crust and mantle heterogeneity on PP/P and SS/S amplitude ratios, *Geophys. Res. Lett.*, **29**, 1430, doi:10.1029/2001GL013831.
- Ritsema, J., van Heijst, H.-J., Woodhouse, J.H. & Deauss, A., 2009. Long-period body-wave traveltimes through the crust: implication for crustal corrections and seismic tomography, *Geophys. J. Int.*, **179**, 1255–1261.

- Ritsema, J., van Heijst, H.J., Deuss, A. & Woodhouse, J.H., 2011. S40RTS: a degree-40 shear-velocity model for the mantle from new Rayleigh wave dispersion, teleseismic traveltimes, and normal-mode splitting function measurements, *Geophys. J. Int.*, **184**, doi:10.1111/j.1365-246X.2010.04884.x.
- Ritzwoller, M.H. & Lavelle, E.M., 1995. Three-dimensional models of the Earth's mantle, *Reviews of Geophysics*, **33**, 1–66.
- Rudolph, M.L., Lekić, V. & Lithgow-Bertelloni, C., 2016. Viscosity jump in Earth's mid-mantle, *Science*, **360**(6266), 1349–1352.
- Schaeffer, A.J. & Lebedev, S., 2013. Global shear speed structure of the upper mantle and transition zone, *Geophys. J. Int.*, **194**, 417–449.
- Sengupta, M. & Toksöz, N., 1977. Three-dimensional model of seismic velocity variation in the Earth's mantle, *Geophys. Res. Lett.*, **3**, 84–86.
- Shapiro, N.M. & Ritzwoller, M., 2002. Monte-Carlo inversion for a global shear-velocity model of the crust and upper mantle, *Geophys. J. Int.*, **151**, 88–105.
- Simons, F.J., Nolet, G., Georgief, P., Babcock, J.M., Regier, L.A. & Davis, R.E., 2009. On the potential of recording earthquakes for global seismic tomography by low-cost autonomous instruments in the oceans, *J. geophys. Res.*, **114**, B05307, doi:10.1029/2008JB006088.
- Smith, R.B. & Braile, L.W., 1994. The yellowstone hotspot, *J. Volcanol. Geotherm. Res.*, **61**, 121–187.
- Snieder, R., 1993. Global inversions using normal mode and long-period surface waves, in *Seismic Tomography: Theory and Practice*, pp. 22–63, eds Iyer, H.M. & Hirahara, K., Chapman and Hall.
- Song, T.A. & Kawakatsu, H., 2012. Subduction of oceanic asthenosphere: Evidence from sub-slab seismic anisotrop, *Geophys. Res. Lett.*, **39**, L17301, doi:10.1029/2012GL052639.
- Spakman, W., der Lee, S.V. & der Lee, R.V., 1993. Travel-time tomography of the European-Mediterranean mantle down to 1400 km, *Phys. Earth planet. Inter.*, **79**, 3–74.
- Spetzler, J., Trampert, J. & Snieder, R., 2001. Are we exceeding the limits of the great circle approximation in global surface wave tomography?, *Geophys. Res. Lett.*, **28**, 2341–2344.
- Sukhovich, A., Bonnivieux, S., Hello, Y., Irisson, J.-O., Simons, F.J. & Nolet, G., 2015. Seismic monitoring in the oceans by autonomous floats, *Nat. Commun.*, **6**, 8027, doi:10.1038/ncomms9027.
- Talagrand, O. & Courtier, P., 1987. Variational assimilation of meteorological observations with the adjoint vorticity equation. I: Theory, *Q. J. R. Meteorol. Soc.*, **113**, 1311–1328.
- Tape, C., Liu, Q. & Tromp, J., 2007. Finite-frequency tomography using adjoint methods—Methodology and examples using membrane surface waves, *Geophys. J. Int.*, **168**, 1105–1129.
- Tape, C., Liu, Q., Maggi, A. & Tromp, J., 2009. Adjoint tomography of the Southern California crust, *Science*, **325**, 988–992.
- Tape, C., Liu, Q., Maggi, A. & Tromp, J., 2010. Seismic tomography of the southern California crust based on spectral-element and adjoint methods, *Geophys. J. Int.*, **180**, 433–462.
- Tarantola, A., 1984a. Linearized inversion of seismic reflection data, *Geophys. Prospect.*, **32**, 998–1015.
- Tarantola, A., 1984b. Inversion of seismic reflection data in the acoustic approximation, *Geophysics*, **49**(8), 1259–1266.
- Tarantola, A., 1988. Theoretical background for the inversion of seismic waveforms, including elasticity and attenuation, *Pure appl. Geophys.*, **128**, 365–399.
- Thomas, T., Livermore, R. & Pollitz, F., 2003. Motion of the Scotia Sea Plates, *Geophys. J. Int.*, **155**(3), 789–804.
- Trampert, J. & Snieder, R., 1996. Model estimations biased by truncated expansions: possible artifacts in seismic tomography, *Science*, **271**, 1257–1260.
- Trampert, J. & Woodhouse, J.H., 1995. Global phase velocity maps of Love and Rayleigh waves between 40 and 150 seconds, *Geophys. J. Int.*, **122**, 675–690.
- Trampert, J. & Woodhouse, J.H., 2001. Assessment of global phase velocity models, *Geophys. J. Int.*, **144**, 165–174.
- Trampert, J. & Woodhouse, J.H., 2003. Global anisotropic phase velocity maps for fundamental mode surface waves between 40 and 150 s, *Geophys. J. Int.*, **154**, 154–165.
- Tromp, J., Tape, C. & Liu, Q., 2005. Seismic tomography, adjoint methods, time reversal and banana-doughnut kernels, *Geophys. J. Int.*, **160**(1), 195–216.
- Tromp, J., Komatsitsch, D. & Liu, Q., 2008. Spectral-element and adjoint methods in seismology, *Commun. Comput. Phys.*, **3**(1), 1–32.
- Tromp, J. et al., 2010. Near real-time simulations of global CMT earthquakes, *Geophys. J. Int.*, **183**, 381–389.
- Valentine, A. & Trampert, J., 2016. The impact of approximations and arbitrary choices on geophysical images, *Geophys. J. Int.*, **204**, 59–73.
- van der Hilst, R., Widjiantoro, S. & Engdahl, E.R., 1997. Evidence of deep mantle circulation from global tomography, *Nature*, **386**, 578–584.
- Virieux, J. & Operto, S., 2009. An overview of full-waveform inversion in exploration geophysics, *Geophysics*, **74**(6), WCC1–WCC26.
- Wang, Z. & Dahlen, F.A., 1995. Spherical-spline parameterization of three-dimensional Earth, *Geophys. Res. Lett.*, **22**, 3099–3102.
- Woodhouse, J.H. & Dziewoński, A.M., 1984. Mapping the upper mantle: Three-dimensional modeling of Earth structure by inversion of seismic waveforms, *J. geophys. Res.*, **89**, 5953–5986.
- Woodhouse, J.H. & Girnus, T.P., 1982. Surface waves and free oscillations in a regional earth model, *Geophys. J. R. astr. Soc.*, **68**, 653–675.
- Yuan, Y.O. & Simons, F.J., 2014. Multiscale adjoint waveform-difference tomography using wavelets, *Geophysics*, **79**(3), 79–95.
- Yuan, Y.O., Simons, F.J. & Bozdağ, E., 2015. Multiscale adjoint waveform tomography for surface and body waves, *Geophysics*, **80**(5), R281–R302.
- Yuan, Y.O., Simons, F.J. & Tromp, J., 2016. Double-difference adjoint seismic tomography, *Geophys. J. Int.*, **206**, 1599–1618.
- Zhao, L., Jordan, T.H. & Chapman, C.H., 2000. Three-dimensional Fréchet differential kernels for seismic delay times, *Geophys. J. Int.*, **141**, 558–576.
- Zhou, H.W., 1996. A high resolution P wave model of the top 1200 km of the mantle, *J. geophys. Res.*, **101**, 27 791–27 810.
- Zhou, Y., Dahlen, F.A. & Nolet, G., 2004. Three-dimensional sensitivity kernels for surface wave observables, *Geophys. J. Int.*, **158**, 142–168.
- Zhou, Y., Nolet, G., Dahlen, F.A. & Laske, G., 2006. Global upper-mantle structure from finite-frequency surface-wave tomography, *J. geophys. Res.*, **111**, B04304, doi:10.1029/2005JB003677.
- Zhou, Y., Liu, Q. & Tromp, J., 2011. Surface-wave sensitivity: Mode summation versus adjoint SEM, *Geophys. J. Int.*, **187**, 142–168.
- Zhu, H. & Tromp, J., 2013. Mapping tectonic deformation in the crust and upper mantle beneath Europe and the North Atlantic Ocean, *Science*, **341**, 871–875.
- Zhu, H., Bozdağ, E., Peter, D. & Tromp, J., 2012. Structure of the European upper mantle revealed by adjoint tomography, *Nature Geosciences*, **5**, 493–498.
- Zhu, H., Bozdağ, E., Duffy, T.S. & Tromp, J., 2013. Seismic attenuation beneath Europe and the North Atlantic: implications for water in the mantle, *Earth planet. Sci. Lett.*, **381**, 1–11.
- Zhu, H., Bozdağ, E. & Tromp, J., 2015. Seismic structure of the European upper mantle based on adjoint tomography, *Geophys. J. Int.*, **201**, 18–52.